PLOS BIOLOGY

RESEARCH ARTICLE

Structural basis of DSF recognition by its receptor RpfR and its regulatory interaction with the DSF synthase RpfF

Evan J. Waldron[1], Daniel Snyder[2], Nicolas L. Fernandez[3], Emily Sileo[2], Daigo Inoyama[4], Joel S. Freundlich[4], Christopher M. Waters[3], Vaughn S. Cooper[2], Matthew B. Neiditch[1]*

1 Department of Microbiology, Biochemistry, and Molecular Genetics, New Jersey Medical School, Rutgers, State University of New Jersey, Newark, New Jersey, United States of America, **2** Department of Microbiology and Molecular Genetics, and Center for Evolutionary Biology and Medicine, University of Pittsburgh, Pittsburgh, Pennsylvania, United States of America, **3** Department of Microbiology and Molecular Genetics and the BEACON Center for the Study of Evolution in Action, Michigan State University, East Lansing, Michigan, United States of America, **4** Department of Pharmacology, Physiology, and Neuroscience, New Jersey Medical School, Rutgers, State University of New Jersey, Newark, New Jersey, United States of America

* matthew.neiditch@rutgers.edu

OPEN ACCESS

Citation: Waldron EJ, Snyder D, Fernandez NL, Sileo E, Inoyama D, Freundlich JS, et al. (2019) Structural basis of DSF recognition by its receptor RpfR and its regulatory interaction with the DSF synthase RpfF. PLoS Biol 17(2): e3000123. https://doi.org/10.1371/journal.pbio.3000123

Academic Editor: Robert B. Bourret, University of North Carolina, UNITED STATES

Received: September 28, 2018

Accepted: January 10, 2019

Published: February 4, 2019

Data Availability Statement: Atomic coordinates and structure factors for RpfRCt(FI), RpfRCt(FI)-RpfFBc, RpfRCt(PAS)-C12:0, and RpfRCt(PAS)-BDSF have been deposited in the Protein Data Bank under accession codes 6DGA, 6DGN, 6DGG, and 6DGJ.

Funding: EJW, DS, NF, ES, EM, CMW, VSC, and MBN were funded by National Institutes of Health R01 GM110444; MBN was funded by National Institutes of Health R01 AI125452; and EJW was funded by National Institutes of Health T32

Abstract

The diffusible signal factors (DSFs) are a family of quorum-sensing autoinducers (AIs) produced and detected by numerous gram-negative bacteria. The DSF family AIs are fatty acids, differing in their acyl chain length, branching, and substitution but having in common a *cis*-2 double bond that is required for their activity. In both human and plant pathogens, DSFs regulate diverse phenotypes, including virulence factor expression, antibiotic resistance, and biofilm dispersal. Despite their widespread relevance to both human health and agriculture, the molecular basis of DSF recognition by their cellular receptors remained a mystery. Here, we report the first structure–function studies of the DSF receptor regulation of pathogenicity factor R (RpfR). We present the X-ray crystal structure of the RpfR DSF-binding domain in complex with the *Burkholderia* DSF (BDSF), which to our knowledge is the first structure of a DSF receptor in complex with its AI. To begin to understand the mechanistic role of the BDSF–RpfR contacts observed in the biologically important complex, we have also determined the X-ray crystal structure of the RpfR DSF-binding domain in complex with the inactive, saturated isomer of BDSF, dodecanoic acid (C12:0). In addition to these ligand–receptor complex structures, we report the discovery of a previously overlooked RpfR domain and show that it binds to and negatively regulates the DSF synthase regulation of pathogenicity factor F (RpfF). We have named this RpfR region the RpfF interaction (FI) domain, and we have determined its X-ray crystal structure alone and in complex with RpfF. These X-ray crystal structures, together with extensive complementary in vivo and in vitro functional studies, reveal the molecular basis of DSF recognition and the importance of the *cis*-2 double bond to DSF function. Finally, we show that throughout cellular growth, the production of BDSF by RpfF is post-translationally controlled by the RpfR N-terminal FI domain, affecting the cellular concentration of the bacterial second messenger bis-(3′-5′)-cyclic dimeric guanosine monophosphate (c-di-GMP). Thus, in addition to describing

AI125185 (www.nih.gov). The funders had no role in study design, data collection and analysis, decision to publish, or preparation of the manuscript.

Competing interests: The authors have declared that no competing interests exist.

Abbreviations: ACP, acyl carrier protein; AI, autoinducer; Arg, arginine; Asn, asparagine; BDSF, *Burkholderia* DSF; BLASTP, protein BLAST; C3, carbon 3; C12:0, dodecanoic acid; C12:0–ACP_{Ec}, C12:0-charged ACP_{Ec}; c-di-GMP, bis-(3′-5′)-cyclic dimeric guanosine monophosphate; Cache, Ca^{2+}channels-chemotaxis receptors; CoA, Coenzyme A; DGC, diguanylate cyclase; DSF, diffusible signal factors; FI, RpfF interaction; LC-MS, Liquid chromatography–mass spectrometry; GAF, cyclic GMP-specific phosphodiesterase-adenylyl cyclase-FhlA; GMP, guanosine monophosphate; gmr, Gene modulating RNase II; holo-ACP_{Ec}, *E. coli* 4′-phosphopantetheinyl ACP; PAS, Per-Arnt-Sim; PDB, Protein Data Bank; PDE, phosphodiesterase; PDSF, *Pseudomonas* DSF; pGpG, 5′-phosphoguanylyl-(3′,5′)-guanosine; Phe, phenylalanine; RbdA, Regulator of biofilm dispersal of Pseudomonas aeruginosa; RpfB, regulation of pathogenicity factor B; RpfF, regulation of pathogenicity factor F; RpfR, regulation of pathogenicity factor R; SAD, single-wavelength anomalous dispersion; SUMO, small ubiquitin-like modifier.

the molecular basis for the binding and specificity of a DSF for its receptor, we describe a receptor–synthase interaction regulating bacterial quorum-sensing signaling and second messenger signal transduction.

Author summary

Communication between many species of gram-negative bacteria is mediated by a family of cell–cell signaling autoinducers (AIs) known as the diffusible signal factors (DSFs). DSFs are fatty acids, containing a signature *cis*-2 double bond critical for their activity. The DSFs differ from one another by their acyl chain length, branching, and the presence of additional double bonds. We have carried out the first structure–function studies of DSF binding to a receptor, regulation of pathogenicity factor R (RpfR). We have determined X-ray crystal structures of the RpfR DSF-binding domain in complex with an active DSF, *cis*-2-dodecenoic acid, and in complex with its inactive saturated isomer, dodecanoic acid (C12:0). These X-ray crystal structures, together with extensive complementary in vivo and in vitro functional studies, reveal the molecular basis of DSF recognition and the importance of the *cis*-2 double bond to DSF function. In addition, we have discovered a previously overlooked domain at the RpfR N-terminus, and we show that this domain binds to and negatively regulates the DSF synthase regulation of pathogenicity factor F (RpfF). We present X-ray crystal structures of this domain alone and in complex with RpfF, which—together with in vivo and in vitro functional studies—describe how RpfR binds to RpfF, negatively regulating the synthesis of its own AI.

Introduction

Quorum sensing is a form of bacterial cell–cell communication that enables populations of bacteria to synchronize their gene expression in order to coordinate group behaviors such as bioluminescence, sporulation, genetic competence, biofilm formation, motility, and virulence factor expression (reviewed in [1,2]). Quorum sensing is mediated by signaling molecules known as autoinducers (AIs) that bacteria secrete and detect. While gram-positive bacteria communicate using peptide AIs (reviewed in [3,4]), gram-negative bacteria use a panoply of small molecule AIs, including the diffusible signal factors (DSFs) (reviewed in [5]), which are the focus of the studies presented here.

DSFs (Fig 1A) are a family of fatty acid AIs produced and detected by a wide range of gram-negative bacteria, including important pathogens [6]. DSFs regulate virulence factor expression, antibiotic resistance, and additional traits important for adaptation within biofilms and biofilm-associated infections [7–11]. While DSFs can differ in their acyl chain length, branching, and substitution, a common chemical feature shared among all DSFs is a *cis*-2 double bond, which is required for signaling activity (reviewed in [12]). The commonality of the *cis*-2 double bond as well as the structural diversity in DSFs is evident when comparing the canonical DSF (*cis*-11-methyl-2-dodecenoic acid), which was discovered in *Xanthomonas campestris* pv. *campestris*, with both the *Burkholderia* DSF (BDSF) (*cis*-2-dodecenoic acid), which was first identified in *Burkholderia cenocepacia*, and the *Pseudomonas* DSF (PDSF) (*cis*-2-decenoic acid), which was discovered in *Pseudomonas aeruginosa* (Fig 1A) [7,13,14].

The enzyme RpfF catalyzes the synthesis of DSF family signals through the dehydration of 3-hydroxyacyl thioesters attached to acyl carrier protein (ACP), producing the *cis*-2 double

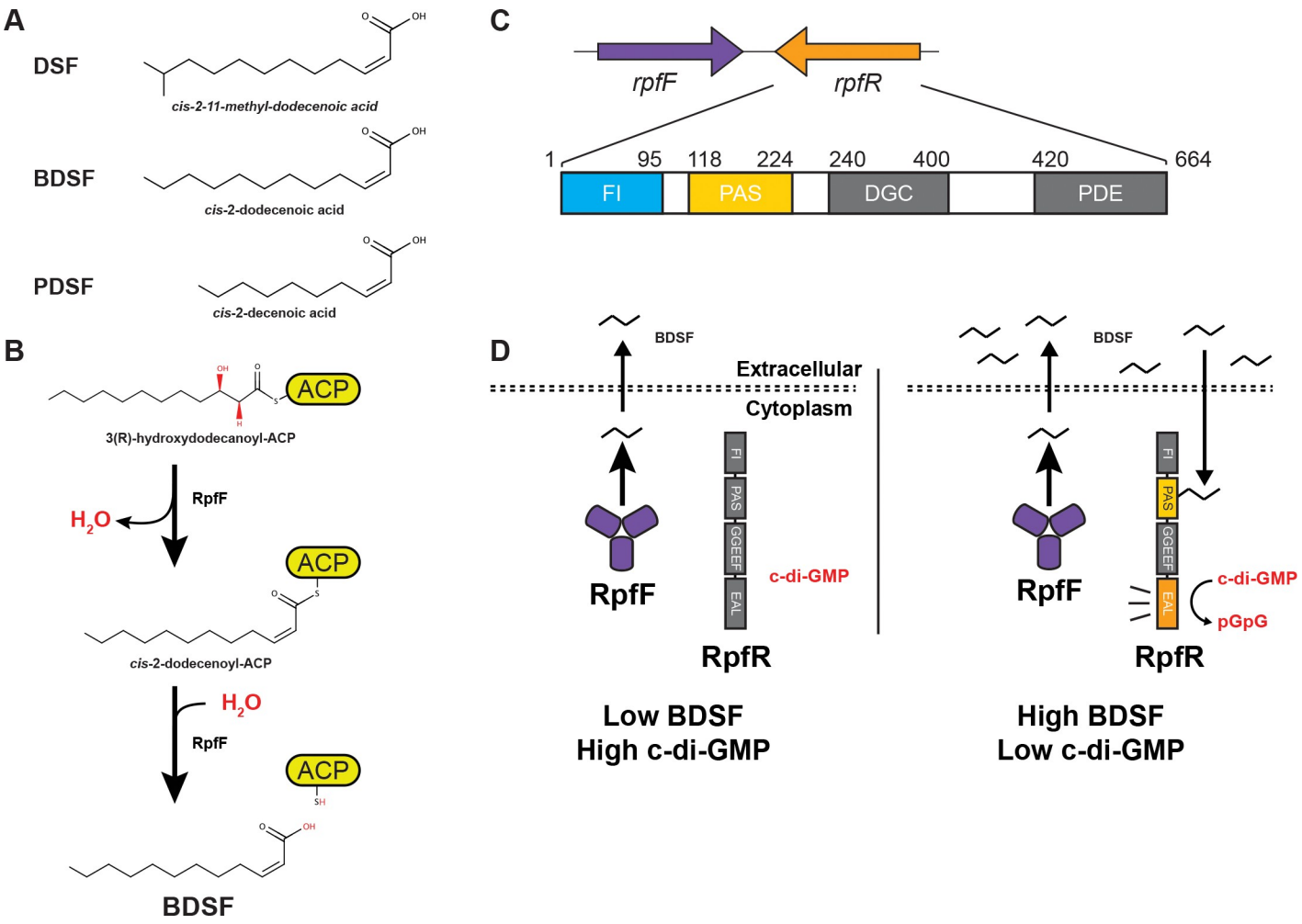

Fig 1. Synthesis and detection of DSF AIs. (A) Structure of DSF (*cis*-2-11-methyl-dodecenoic acid), BDSF (*cis*-2-dodecenoic acid), and PDSF (*cis*-2-decenoic acid). (B) RpfF synthesizes BDSF in a two-step mechanism. RpfF dehydrates 3-hydroxydodecanoyl-ACP to form the *cis*-2-dodecenoyl-ACP. RpfF hydrolyzes the thioester bond linking the acyl-chain to ACP, releasing holo-ACP and free BDSF. (C) Schematic representation of RpfR. (Top) The genomic orientation of *rpfF and rpfR* show that they are convergently transcribed. (Bottom) A schematic representation of $RpfR_{Ct}$. The FI domain (residues 1–95) and PAS domain (residues 118–224) are depicted in blue and yellow, respectively. The approximate positions of the DGC and PDE domains (gray) were determined by sequence homology. Linker regions between domains are shown in white. (D) Previously established BDSF-signaling model. (Left panel) At low levels of BDSF, RpfR PDE activity is low and c-di-GMP levels are high. (Right panel) At elevated concentrations, BDSF binds to the RpfR PAS domain, triggering RpfR PDE-mediated hydrolysis of c-di-GMP to pGpG. ACP, acyl carrier protein; AI, autoinducer; BDSF, *Burkholderia* DSF; c-di-GMP, bis-(3′-5′)-cyclic dimeric guanosine monophosphate; DGC, diguanylate cyclase; DSF, diffusible signal factor; FI, RpfF interaction; PAS, Per-Arnt-Sim; PDE, phosphodiesterase; PDSF, *Pseudomonas* DSF; pGpG, 5′-phosphoguanylyl-(3′,5′)-guanosine; RpfF, regulation of pathogenicity factor F; RpfR, regulation of pathogenicity factor R.

https://doi.org/10.1371/journal.pbio.3000123.g001

bond (Fig 1B). Subsequent hydrolysis of the *cis*-2 acyl thioester by RpfF releases the free fatty acid DSF AI from ACP [15,16]. While structural studies have examined DSF synthesis [17–19], the structural basis of DSF–receptor interactions are unexplored.

The DSF receptor RpfR is conserved in numerous gram-negative bacteria, including, among others, *Escherichia coli*, *B. cenocepacia*, *Cronobacter turicensis*, *Serratia marcescens*, *Yersinia enterocolitica*, and *Enterobacter cloacae*. RpfR was predicted to contain three domains, namely Per-Arnt-Sim (PAS), diguanylate cyclase (DGC), and phosphodiesterase (PDE) domains (Fig 1C) [20–22]. PAS domains are ligand-binding domains present in all kingdoms of life, and they are capable of detecting a multitude of signals, including small molecules, light, redox, as well as the conformational state of other proteins (reviewed in [23,24]).

Therefore, the RpfR PAS domain was predicted to bind DSF [22]. DGC domains, such as that found in RpfR, produce the bacterial second messenger bis-(3′-5′)-cyclic dimeric guanosine monophosphate (c-di-GMP), whose increased concentration is associated with biofilm formation and sessile behavior. PDE domains hydrolyze c-di-GMP to linear 5′-phosphoguanylyl-(3′,5′)-guanosine (pGpG), reducing the cellular concentration of c-di-GMP, which commonly triggers biofilm dispersal and virulence factor expression (reviewed in [25]). BDSF binding to RpfR was previously shown to trigger its PDE activity, decreasing the intracellular concentration of c-di-GMP and favoring biofilm dispersal (Fig 1D) [20,22].

Here, we present a structure–function analysis of RpfR, revealing detailed mechanistic insight into DSF sensing. Additionally, we identified receptor-mediated control of DSF production via a direct interaction of RpfR with the DSF synthase RpfF. The foundation of this work are four X-ray crystal structures. The first two structures presented are those of the RpfR PAS domain in complex with BDSF or the saturated inactive isomer of BDSF, dodecanoic acid (C12:0). Structural comparison of these models along with in vivo functional analysis reveals the molecular basis for BDSF-binding specificity and the role of the DSF *cis*-2 double bond in signal perception. Additionally, we discovered that in contrast to prior predictions [22], RpfR in fact contains an overlooked N-terminal domain that binds to RpfF, inhibiting DSF synthesis. Consistent with its function, we refer to the RpfR N-terminal domain as the RpfF interaction (FI) domain. To explore the mechanism of RpfR-mediated RpfF inhibition, we determined the X-ray crystal structures of the RpfR FI domain alone and in complex with RpfF. These crystal structures, along with extensive in vivo and in vitro studies, reveal the mechanistic basis of this regulation and its contribution to restraining BDSF synthesis and elevating the intracellular concentration of c-di-GMP. Since DSF signaling commonly regulates cellular behaviors, including biofilm formation, biofilm dispersal, swarming motility, extracellular protease production, antibiotic resistance, and other virulence-associated phenotypes in important human and plant pathogens [9,20,26–32], the mechanistic insight into DSF sensing and synthesis presented here set the stage for developing inhibitors important for human health and agriculture.

Results

Structure of the RpfR PAS domain bound to dodecanoic acid

To gain insight into the molecular recognition of BDSF by RpfR, we crystallized and determined the structure of the *C. turicensis* RpfR PAS domain (Fig 2A, S1 Table). Without adding fatty acid to the crystallization experiment, we observed prominent electron density in the PAS domain core that was consistent with a 12-carbon fatty acid ligand (Fig 2A–2C). Intriguingly, even when an excess of BDSF was included during crystallization, the electron density was consistent with a fatty acid that did not contain a *cis-2* double bond (Fig 2C). These data suggested that $RpfR_{Ct}$(PAS) copurified with a tightly bound fatty acid likely originating from the *E. coli* overexpression host. Indeed, using liquid chromatography–mass spectrometry (LC-MS), we determined that the ligand is the saturated isomer of BDSF, C12:0 (S1 Fig), which *E. coli* is known to produce endogenously [33]. Thus, we built and refined the 1.5 Å resolution X-ray crystal structure of $RpfR_{Ct}$(PAS)–C12:0 (Fig 2A–2C).

While C12:0 is an inactive isomer of BDSF, the $RpfR_{Ct}$(PAS)–C12:0 structure provided the first insight into how fatty acids interact with RpfR and, as shown below, proved to be important for comparative analysis. In the $RpfR_{Ct}$(PAS)–C12:0 structure, the C12:0 carboxylic acid group forms multiple hydrogen bonds with a set of conserved hydrophilic residues (S169, N172, Y183, and R187) at one end of the ligand-binding pocket (Fig 2B). At the other end of the pocket, the C12:0 hydrophobic acyl tail is surrounded by conserved hydrophobic residues

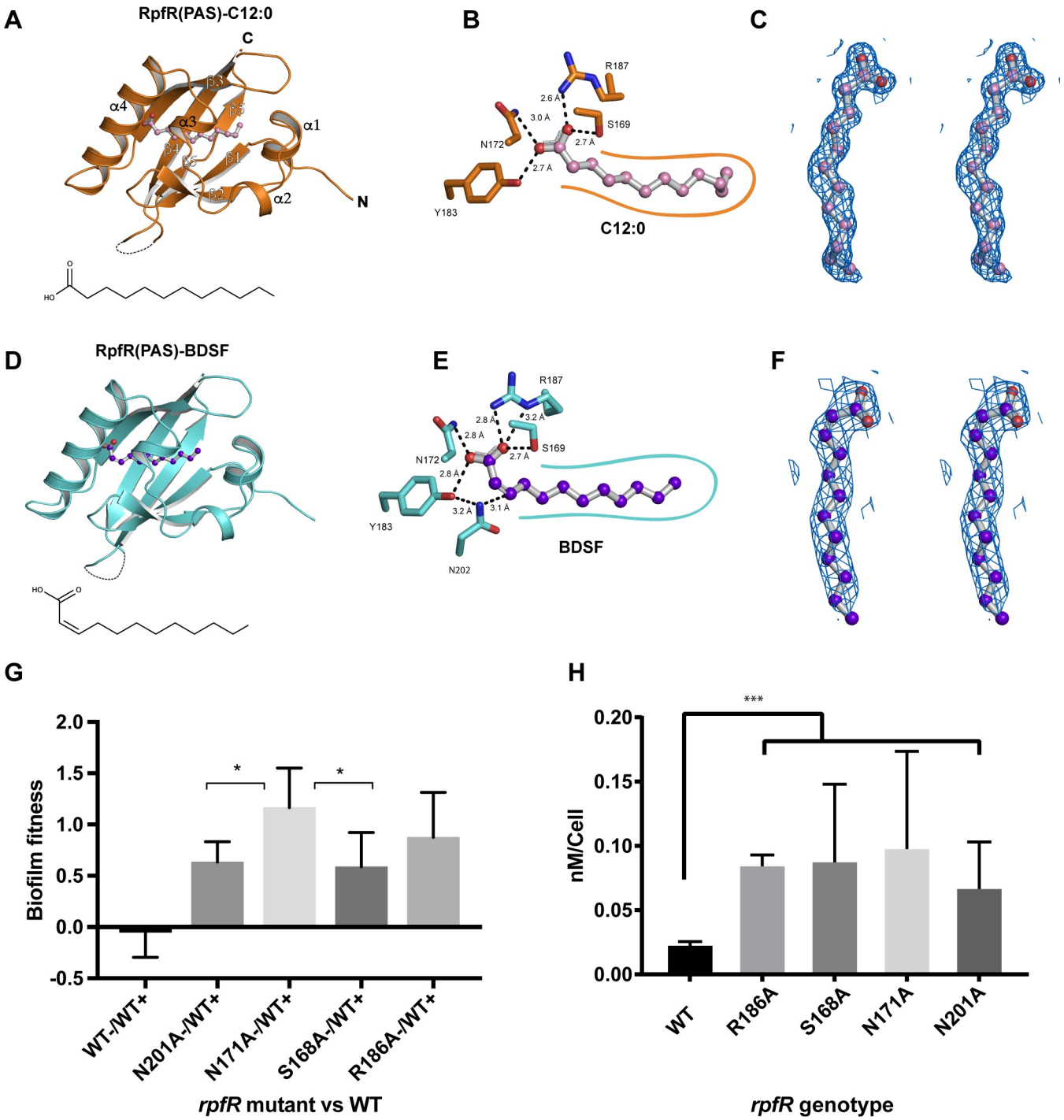

Fig 2. The X-ray crystal structures for RpfR$_{Ct}$(PAS)–C12:0 and RpfR$_{Ct}$(PAS)–BDSF. (A) Cartoon representation of RpfR$_{Ct}$(PAS) (orange) in complex with C12:0 (pink/red balls and gray sticks). Disordered residues 207–212 are shown as a dashed line. C12:0 alone is depicted in the same orientation as the bound ligand below the model. (B) C12:0 (pink/red balls and gray sticks) interacting with the hydrophilic RpfR$_{ct}$(PAS)-binding site residues (orange sticks). Hydrogen bonds (black dashed lines) between hydrophilic residues and the C12:0 carboxylic acid group are shown with their measured distances. RpfR–C12:0 hydrophobic interactions are depicted as a smooth orange contour line. (C) Stereo diagram of C12:0 (pink/red balls and gray sticks) and corresponding $2F_o$-F_c electron density contoured at 1.0 σ. (D) Cartoon representation of RpfR$_{ct}$(PAS) (cyan) in complex with BDSF (purple/red balls and gray sticks). Disordered residues 206–212 are shown as a dashed line. Below the structure, BDSF alone is depicted in the same orientation of the modeled ligand. (E) BDSF (purple/red balls and gray sticks) forming hydrogen bonds (black dashed lines with their measured distances) with the same RpfR$_{ct}$(PAS)-binding site residues as C12:0. N202 forms an additional interaction with C3 of BDSF. R187 forms an additional hydrogen bond with the BDSF carboxylic acid. RpfR–BDSF hydrophobic interactions are depicted as a smooth cyan contour line. (F) Stereo diagram of BDSF and corresponding $2F_o$-F_c electron density contoured at 1.0 σ (purple/red

balls and gray sticks). (G) Biofilm fitness advantages of *B. cenocepacia* strains containing chromosomally encoded $RpfR_{Bc}$ BDSF-binding site point mutations in direct competition with WT strain HI2424. Fitness is the difference in selective rate constants (*s*) over 24 h of attachment and biofilm assembly on a polystyrene bead. Each mutant is significantly more fit than WT (ANOVA with Tukey posthoc testing, $P < 0.001$), and N171A is more fit than N201A or S168A ($P < 0.05$) [34,35]. (H) Measurement of the average c-di-GMP pool per cell at 24 h in planktonic cultures of WT *B. cenocepacia* or strains containing $RpfR_{Bc}$ BDSF-binding site point mutants. C-di-GMP levels are significantly greater in the mutant strains than in the WT (***Welch's unpaired *t* test, $P < 0.0006$). The numerical values underlying panels G and H can be found in S1 Data. BDSF, *Burkholderia* DSF; C3, carbon 3; C12:0, dodecanoic acid; c-di-GMP, bis-(3′-5′)-cyclic dimeric guanosine monophosphate; DSF, diffusible signal factor; GMP; PAS, Per-Arnt-Sim; WT, wild-type.

https://doi.org/10.1371/journal.pbio.3000123.g002

(Fig 2A and 2B, S2A Fig). While the $RpfR_{Ct}$(PAS)–C12:0 structure provided insight into RpfR fatty acid binding, a mechanistic understanding of how RpfR recognizes BDSF demanded determination of the bona fide $RpfR_{Ct}$(PAS)–BDSF structure.

Purification and X-ray crystal structure of the RpfR PAS domain–BDSF complex

BDSF was previously demonstrated to trigger $RpfR_{Ct}$ phosphodiesterase activity [20]. To obtain $RpfR_{Ct}$(PAS) bound to the functionally active ligand BDSF, rather than the inactive ligand C12:0, we overexpressed and purified the $RpfR_{Ct}$(PAS) domain from *E. coli* engineered to express BDSF. It is notable that while *E. coli* contains a highly conserved *rpfR* homolog named the gene modulating RNase II (*gmr*), it lacks a DSF synthase and, to our knowledge, does not produce a DSF AI [21,34]. We speculate, however, that *E. coli* Gmr PDE activity could be regulated by C12:0. Regardless, *E. coli* was previously demonstrated to synthesize BDSF when transformed with an expression plasmid containing $rpfF_{Bc}$ [15,30]. Therefore, we purified $RpfR_{Ct}$(PAS) from *E. coli* coexpressing $RpfF_{Bc}$. The purified $RpfR_{Ct}$(PAS) was then denatured and LC-MS used to identify the released ligand (S3 Fig). Indeed, the bound ligand was BDSF, confirming that we had purified the $RpfR_{Ct}$(PAS)–BDSF complex.

The $RpfR_{Ct}$(PAS)–BDSF complex was crystallized and its structure determined to a resolution of 2.3 Å (Fig 2D–2F, S1 Table). Comparison of the $RpfR_{Ct}$(PAS)–BDSF and $RpfR_{Ct}$(PAS)–C12:0 structures reveals that the ligands adopt different conformations, resulting from the absence or presence of the *cis*-2 double bond in C12:0 or BDSF, respectively. Furthermore, while $RpfR_{Ct}$ arginine (Arg) 187 makes a single H-bond to C12:0, it adopts a different rotameric configuration in the presence of BDSF, forming an additional H-bond between its δ nitrogen and the BDSF carboxylic acid (Fig 2B and 2E).

Based on the measured distances and atom types (Fig 2B and 2E), the position of BDSF in the $RpfR_{Ct}$(PAS)-binding pocket appears to be influenced by an interaction between BDSF and the conserved residue asparagine (Asn) 202 (Fig 2E, S2A Fig and S4 Fig). Specifically, we propose that the Asn202 side chain amide nitrogen interacts with the electron deficient C_β (C3) of BDSF. Below, we explore the physiological importance of the $RpfR_{Ct}$(PAS)–BDSF interactions observed in the crystal structure.

Functional studies of BDSF binding to RpfR

Relative to wild-type *B. cenocepacia*, strains with RpfR proteins containing mutations predicted to disrupt the binding of BDSF to $RpfR_{Bc}$(PAS) should be less sensitive to BDSF, exhibit lower PDE activity, display elevated levels of c-di-GMP, and have increased competitive fitness in biofilms due to elevated biofilm production. We engineered mutations $RpfR_{Bc}$–S168A,–N171A,–R186A, and–N201A (corresponding to the above-described and conserved $RpfR_{Ct}$ BDSF-interacting residues S169, N172, R187, and N202 [S2A Fig]) in the chromosomal copy of *rpfR* and competed them 1:1 with wild-type under a daily cycle of biofilm formation, dispersal, and reattachment [10,35]. Consistent with the interactions observed in the $RpfR_{Ct}$(PAS)–BDSF crystal structure, each mutation produced large and significant fitness advantages, with selective

coefficients (*s*) ranging from 0.58 to 1.17 (Fig 2G). Furthermore, each of these mutations resulted in a significant increase in cellular c-di-GMP relative to the wild-type strain (Fig 2H). While it is possible that the site-directed mutations affected RpfR stability and, in turn, the ability of RpfR to respond to BDSF, we found that purified full-length wild-type $RpfR_{Bc}$, $RpfR_{Bc}$–S168A,–N171A,–R186A, and–N201A were comparably soluble (S5 Fig). Finally, in line with the fact that the $RpfR_{Bc}$(PAS) BDSF-binding mutants displayed increased competitive fitness in the in vitro biofilm life cycle assay and elevated levels of c-di-GMP, we note that $RpfR_{Bc}$(PAS) is subject to positive selection under conditions favoring biofilm growth, such as in a cystic fibrosis patient for which increased biofilm production proves advantageous [11].

Identification and crystallization of a previously undescribed RpfR N-terminal domain

Previous studies identified three RpfR domains: PAS, DGC (GGDEF), and PDE (EAL) [20–22] (Fig 1C). We observed that the undescribed region of RpfR (residues 1–117) was highly conserved among all RpfR homologues (S2B Fig). This led us to hypothesize the presence of a new domain located N-terminal to the BDSF-binding PAS domain. Indeed, we found that a construct containing the first 95 residues of $RpfR_{Ct}$ ($RpfR_{Ct}$[1–95]) was soluble and well folded, as determined by size exclusion chromatography (Fig 3A). As described below, $RpfR_{Ct}$(1–95) was amenable to crystallographic analysis.

Structure of the RpfR N-terminal domain

We determined the X-ray crystal structure of the $RpfR_{Ct}$(1–95) to a resolution of 1.2 Å using the single-wavelength anomalous dispersion (SAD) method (Fig 3B, S1 Table). $RpfR_{Ct}$(1–95) adopts a Profilin-like fold consisting of an N-terminal α-helix and a central six-stranded antiparallel β-sheet with a single α-helix connecting β3 to β4 (Fig 3B, S2B Fig and S6A Fig) [36,37]. Distance-matrix alignment (DALI) and PDBeFold searches of the Protein Data Bank (PDB) show the closest $RpfR_{Ct}$(1–95) structural homologues to be PAS, Ca^{2+}channels-chemotaxis receptors (Cache), and cyclic GMP-specific phosphodiesterase-adenylyl cyclase-FhlA (GAF) domains; however, canonical PAS domains contain five-stranded β-sheets (S6B Fig) [23], and Cache domains are periplasmic domain proteins that contain an additional N-terminal α-helix that extends through the membrane [38]. Like $RpfR_{Ct}$(1–95), GAF domains contain six-stranded antiparallel β-sheets [23,39]; however, unlike GAF domain proteins, $RpfR_{Ct}$(1–95) does not possess a pair of interacting α-helices below its β-sheet (S6C Fig).

Consistent with the fact that $RpfR_{Ct}$(1–95) is neither a PAS, Cache, or GAF domain, protein BLAST (BLASTP) searches using the $RpfR_{Ct}$(1–95) and $RpfR_{Bc}$(1–94) amino acid sequences return neither PAS, Cache, nor GAF domain proteins [40]. Based on the above structural and sequence analysis, we conclude that while the RpfR N-terminal domain is structurally similar to PAS, Cache, and GAF domains, it is a new domain with a Profilin-like fold. As detailed below, this RpfR domain binds to and negatively regulates RpfF; thus, we refer to it as the RpfF interaction (FI) domain.

RpfR(FI) interacts with RpfF

Initial evidence suggesting that RpfR(FI) and RpfF interact came from studies in which an $RpfR_{Bc}$ construct containing both the FI and PAS domains ($RpfR_{Bc}$[FI–PAS]) and $RpfF_{Bc}$ were coexpressed in *E. coli* to obtain $RpfR_{Bc}$(FI–PAS) bound to BDSF. As discussed above, $RpfF_{Bc}$ was employed in these experiments because it was previously shown to produce BDSF when overexpressed in *E. coli* [15,30]. During our experiments to obtain BDSF-bound $RpfR_{Bc}$(FI–PAS), $RpfR_{Bc}$(FI–PAS) containing an N-terminal hexahistidine (His_6) affinity tag copurified

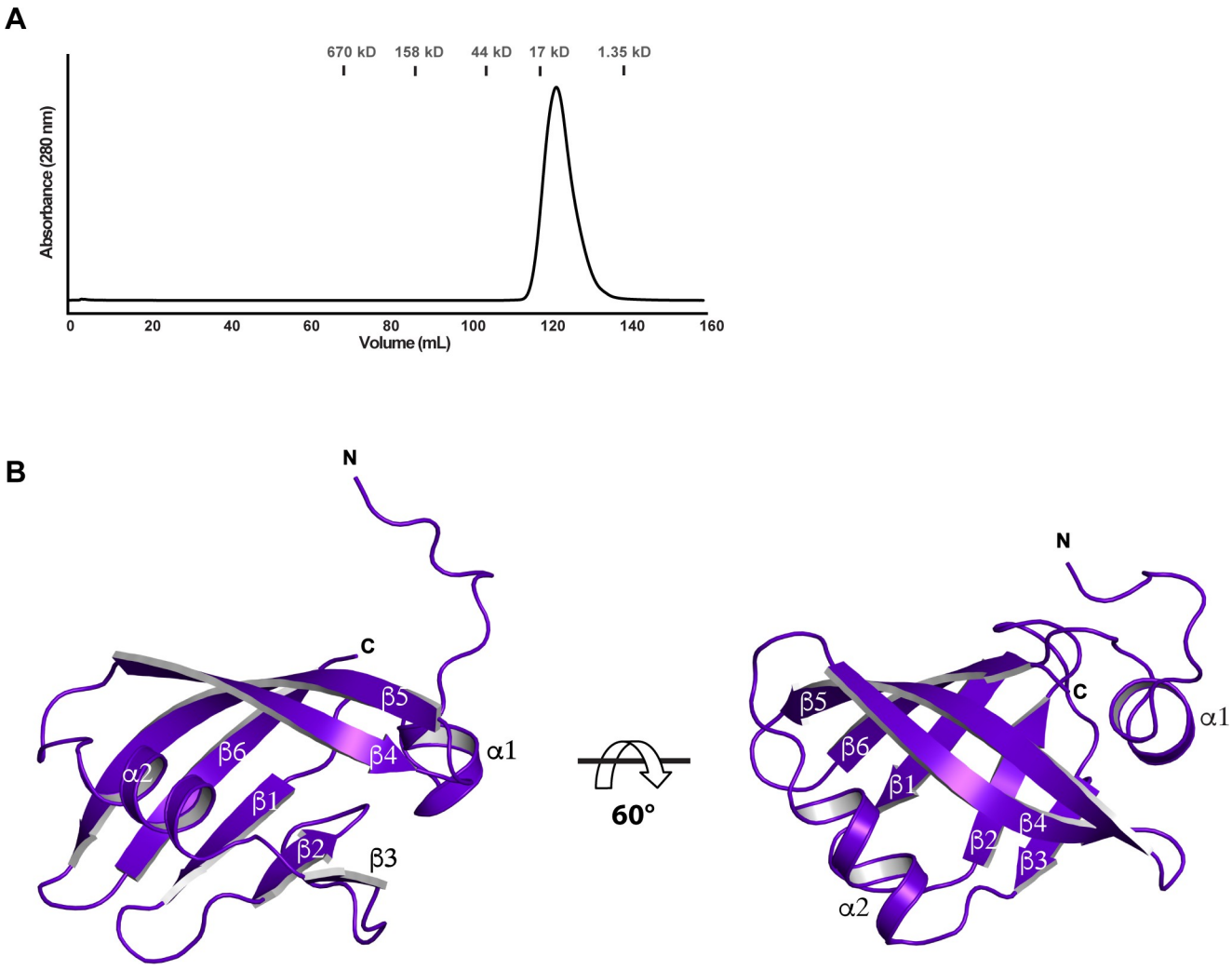

Fig 3. Structure of $RpfR_{Ct}$(FI). (A) A size exclusion chromatogram of $RpfR_{Ct}$(FI). (B) Two views of the $RpfR_{Ct}$(FI) domain are displayed rotated 60˚ from each other along the horizontal axis. Individual secondary structure elements are labeled. FI, RpfF interaction; RpfF, regulation of pathogenicity factor F; RpfR, regulation of pathogenicity factor R.

https://doi.org/10.1371/journal.pbio.3000123.g003

with nontagged $RpfF_{Bc}$ (S7 Fig). As this interaction was not observed when His_6-tagged $RpfR_{Ct}$(PAS) was purified following coexpression with $RpfF_{Bc}$, we hypothesized that $RpfR_{Bc/Ct}$(FI) binds to $RpfF_{Bc}$. To test this hypothesis, we coexpressed $RpfF_{Bc}$ and $RpfR_{Ct}$(FI) and purified the $RpfF_{Bc}$–$RpfR_{Ct}$(FI) complex (Fig 4A).

RpfR(FI) inhibits RpfF thioesterase activity

Based on the fact that RpfR(FI) and RpfF form a complex, we hypothesized that RpfR(FI) regulates RpfF enzymatic activity. To test this hypothesis, we generated *E. coli* 4′-phosphopantetheinyl ACP (holo-ACP_{Ec}) and charged it with C12:0. C12:0-charged ACP_{Ec} (C12:0–ACP_{Ec}) is a substrate for the analysis of in vitro RpfF thioesterase activity [15,17], which we then measured in either the absence or presence of $RpfR_{Bc}$(FI) (Fig 4B). In the absence of $RpfR_{Bc}$(FI), C12:0–ACP_{Ec} was readily converted by $RpfF_{Bc}$ to holo-ACP_{Ec}. In the presence of $RpfR_{Bc}$(FI), conversion of C12:0–ACP_{Ec} substrate by $RpfF_{Bc}$ was significantly reduced (Fig 4B). These results indicate that $RpfR(FI)_{Bc}$ inhibits $RpfF_{Bc}$ thioesterase activity.

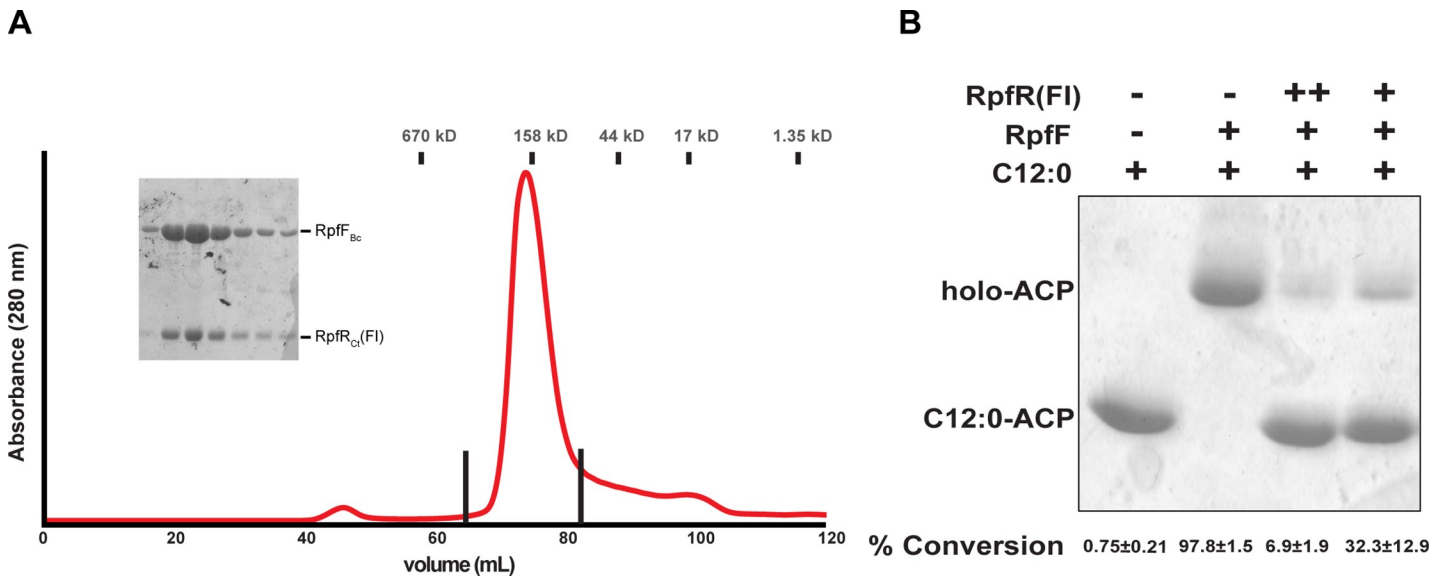

Fig 4. RpfR(FI) binds to RpfF, regulating its thioesterase activity. (A) Size exclusion chromatogram of RpfF$_{Bc}$–RpfR$_{Ct}$(FI). Fractions between the vertical lines were analyzed by 15% SDS-PAGE (inset). The positions of molecular weight standards are indicated above the trace. (B) Conformation sensitive gel electrophoresis of RpfF$_{Bc}$ thioesterase activity in the presence and absence of RpfR$_{Ct}$(FI). The substrate was C12:0–ACP. Average percent conversion of substrate and standard deviation from three separate experiments is shown beneath each lane. The gel shown is a representative example of the three experiments. The numerical values underlying panel B can be found in S1 Data. ACP, acyl carrier protein; C12:0, dodecanoic acid; FI, RpfF, interaction; RpfF, regulation of pathogenicity factor F; RpfR, regulation of pathogenicity factor R.

https://doi.org/10.1371/journal.pbio.3000123.g004

RpfF-RpfR(FI) complex structure

To understand how RpfR(FI) inhibits RpfF thioesterase activity, we determined the RpfF$_{Bc}$–RpfR$_{Ct}$(FI) X-ray crystal structure to a resolution 2.0 Å (Fig 5, S1 Table). RpfF$_{Bc}$–RpfR$_{Ct}$(FI) is a heterohexamer consisting of three RpfR$_{Ct}$(FI) and RpfF$_{Bc}$ protomers. The heterohexamer is generated by 3-fold crystallographic symmetry of the asymmetric unit containing RpfF$_{Bc}$–RpfR$_{Ct}$(FI). Each RpfR$_{Ct}$(FI) protomer simultaneously interacts with two RpfF$_{Bc}$ protomers near their homodimerization interfaces (Fig 5A–5C). This interaction places RpfR(FI)$_{Ct}$ in close proximity to the RpfF$_{Bc}$ substrate tunnel entrance (Fig 5C and 5D). It is also worth noting that the RpfF$_{Bc}$–RpfR$_{Ct}$(FI) interfacial residues are conserved (S2B and S8 Figs), and this interaction is likely common in bacteria encoding both proteins.

When comparing the structure of RpfF$_{Bc}$ alone (PDB:5FUS) [17] with the structure of RpfF$_{Bc}$–RpfR$_{Ct}$(FI), perhaps the most surprising observation is that RpfF$_{Bc}$–RpfR$_{Ct}$(FI) contains no bound fatty acid (S9A Fig). In the previously determined crystal structure of RpfF$_{Bc}$, C12:0 originating from the *E. coli* expression system was identified as a ligand in the RpfF$_{Bc}$ substrate tunnel [17]. Attempts to remove C12:0 prior to biochemical and structural studies were unsuccessful, suggesting that C12:0 may be tightly bound [17]. Consistent with the absence of bound fatty acid in RpfF$_{Bc}$–RpfR$_{Ct}$(FI), structural alignment of RpfF$_{Bc}$–RpfR$_{Ct}$(FI) with RpfF$_{Bc}$ shows that in the complex, phenylalanine (Phe) residues 44 and 88 have adopted a conformation in which they would sterically clash with bound fatty acid if it were present (S9B Fig).

Finally, superposing the structures of RpfR$_{Ct}$(FI) alone with the structure of RpfR$_{Ct}$(FI) in complex with RpfF$_{Bc}$ (Fig 5B) reveals that RpfR$_{Ct}$(FI) undergoes minor conformational changes primarily at the RpfF$_{Bc}$ binding surface. The most significant of these changes occur in RpfR$_{Ct}$(FI) in which the N-terminus of strand β3 extends by one residue, the β2–β3 loop shifts to form contacts with two molecules of RpfF$_{Bc}$ near their homodimerization interface, and the β4–β5 loop becomes

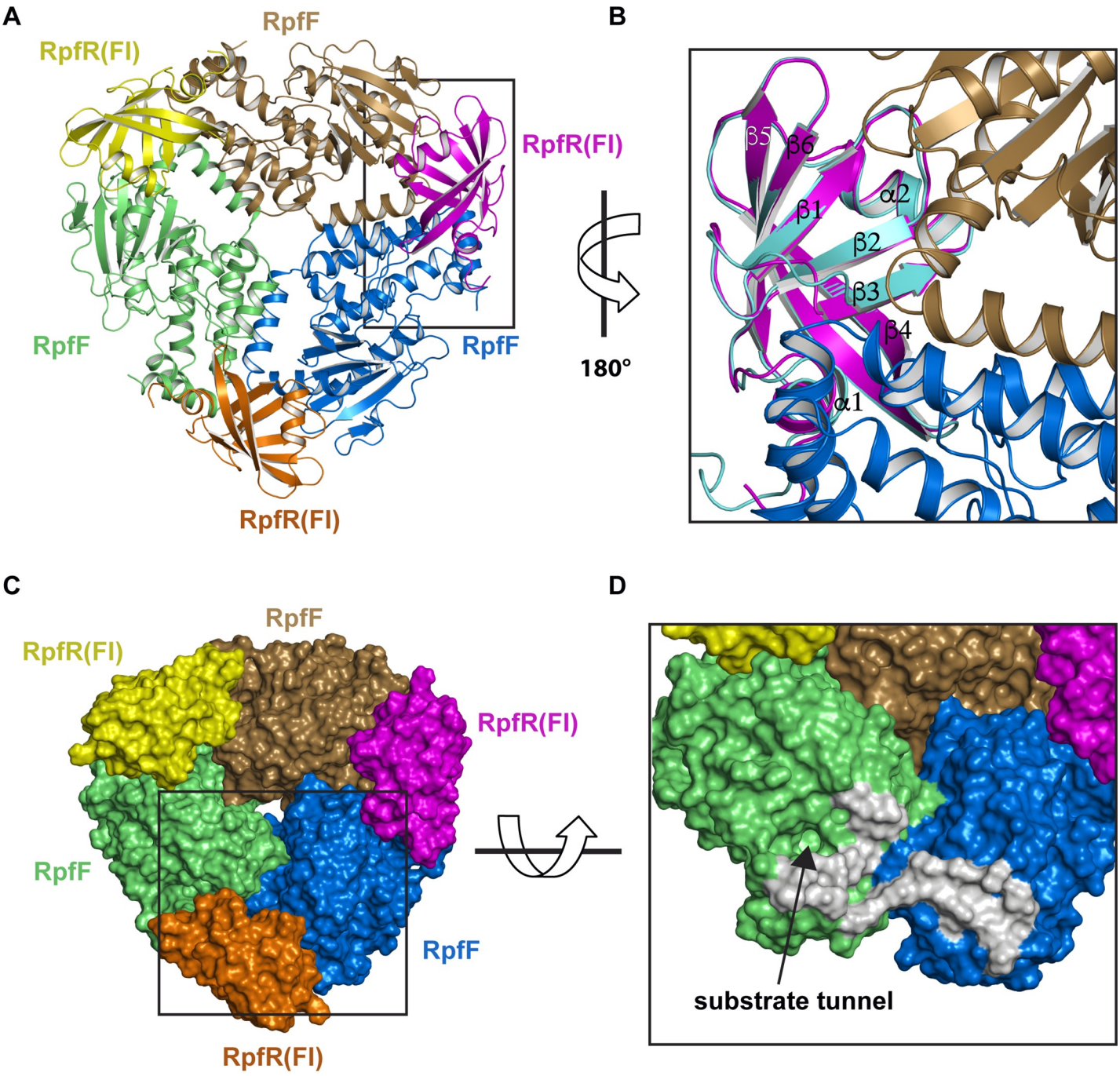

Fig 5. Structure of the $RpfF_{Bc}$–$RpfR_{Ct}$(FI) complex. (A) Cartoon representation of the $RpfF_{Bc}$–$RpfR_{Ct}$(FI) heterohexamer. $RpfF_{Bc}$ monomers are colored lime, sand, and marine. $RpfR_{Ct}$(FI) monomers are colored yellow, magenta, and orange. (B) Expanded (and rotated 180˚) view of the area enclosed by the rectangle in A with the structure of $RpfR_{Ct}$(FI) alone (cyan) aligned with $RpfR_{Ct}$(FI) in complex with $RpfF_{Bc}$ (magenta). (C) Surface representation of the hexamer (colored as in A). (D) Expanded and tilted view of the area enclosed by the rectangle in C orientated looking into the substrate tunnel entrance (for clarity $RpfR_{Ct}$[FI] is omitted). $RpfF_{Bc}$ residues that interact with $RpfR_{Ct}$(FI) are depicted as a gray surface. FI, RpfF interaction; RpfF, regulation of pathogenicity factor F; RpfR, regulation of pathogenicity factor R.

https://doi.org/10.1371/journal.pbio.3000123.g005

buried in the $RpfF_{Bc}$ interface (Fig 5B). Based on the proximity of $RpfR(FI)_{Ct}$ to the $RpfF_{Bc}$ substrate tunnel and its ability to inhibit RpfF thioesterase activity, we propose that $RpfR_{Ct}$(FI) functions to sterically block acyl-ACP substrates from entering the RpfF active site.

RpfR regulates BDSF and c-di-GMP production in vivo

To measure the regulatory effect that RpfR has on RpfF BDSF synthesis in vivo, we employed a *B. cenocepacia* BDSF bioassay and mass spectroscopy to monitor the extracellular accumulation of BDSF in wild-type and mutant strains. More specifically, we compared the extracellular concentration of BDSF in cultures of *B. cenocepacia* strains that were either wild-type (strain HI2424), had the entire *rpfR* gene deleted, or contained an in-frame deletion of the *rpfR* FI domain (Fig 6A and 6B). The *rpfR* and *rpfR* FI domain deletion strains had significantly increased extracellular levels of BDSF compared to the wild-type strain. Consistent with these in vivo BDSF bioassay results and the above biochemical data, the *B. cenocepacia rpfR* deletion

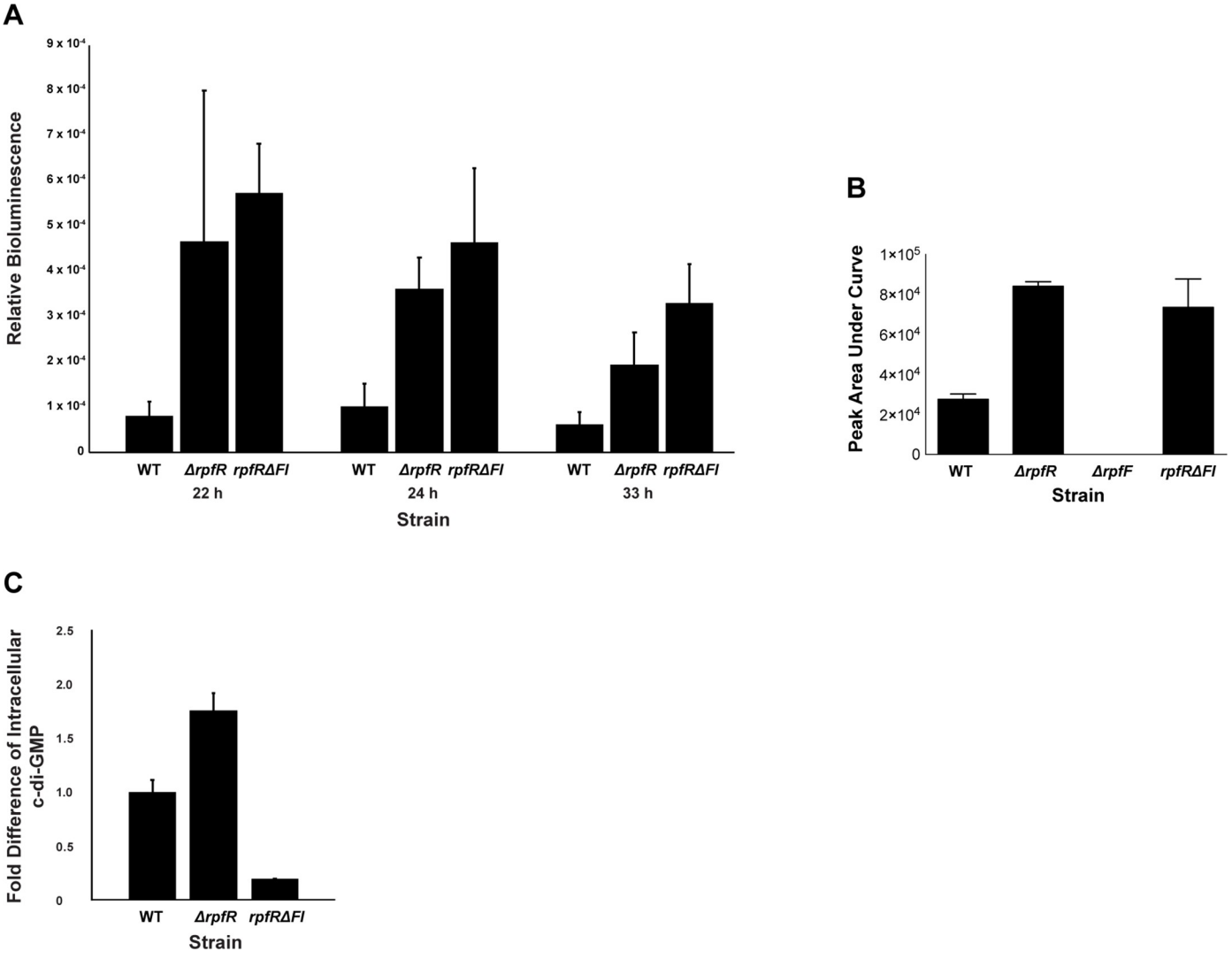

Fig 6. The RpfR FI domain affects the extracellular accumulation of BDSF and the intracellular level of c-di-GMP. (A) The amount of BDSF present in the cell-free supernatant of WT, Δ*rpfR*, and *rpfR*ΔFI truncation *B. cenocepacia* HI2424 strains was measured using the BDSF bioassay. Relative bioluminescence values are shown for times 22 h, 24 h, and 33 h. (B) The amount of BDSF present in the cell-free supernatant of WT, Δ*rpfR*, Δ*rpfF*, and *rpfR*ΔFI truncation *B. cenocepacia* HI2424 strains was measured using mass spectroscopy. $n = 4$, and error bars are 95% confidence intervals. *Indicates a P value $< .05$ determined by one-way ANOVA with Tukey posthoc testing. (C) The fold difference in intracellular c-di-GMP levels in biofilm cells of *B. cenocepacia* HI2424 strains Δ*rpfR* and *rpfR*ΔFI truncation are shown relative to the levels of the WT strain. The numerical values underlying panels A–C can be found in S1 Data. BDSF, *Burkholderia* DSF; c-di-GMP, bis-(3′-5′)-cyclic dimeric guanosine monophosphate; DSF, diffusible signal factor; FI, RpfF interaction; RpfF, regulation of pathogenicity factor F; RpfR, regulation of pathogenicity factor R; WT, wild-type.

https://doi.org/10.1371/journal.pbio.3000123.g006

strain produced elevated levels of c-di-GMP relative to the wild-type strain under biofilm growth conditions, likely resulting from the deletion of the RpfR PDE domain (Fig 6C). Moreover, the RpfR FI domain deletion strain displayed significantly reduced levels of c-di-GMP, consistent with the elevated levels of BDSF stimulating RpfR PDE activity.

Discussion

The role of the BDSF *cis*-2 double bond

The defining feature of the DSF family of AIs that distinguishes them from other fatty acids is their *cis*-2 double bond (Fig 1A) [12]. The *cis*-2 double bond dramatically affects DSF receptor–binding affinity and biological activity. BDSF was shown to tightly bind $RpfR_{Bc}$ (K_d = 877 nM), while C12:0 (K_d = 800 μM) and *trans*-2 dodecenoic acid (K_d = 150 μM) were found to weakly interact with the receptor [22]. Consistent with these results, BDSF was active in a *B. cenocepacia* BDSF bioassay, while C12:0 and *trans*-2 dodecenoic acid were inactive [41]. Despite great interest in DSF-signaling systems, the mechanism of molecular recognition employed by DSF receptors such as RpfR to distinguish DSF AIs from other cellular fatty acids, including the *trans*-2 and saturated isomers of DSF AIs, was unknown. As detailed below, we propose that the BDSF *cis*-2 double bond establishes $RpfR_{Ct}$-binding specificity and affinity by enabling unique ligand–receptor contacts and, in contrast to more flexible fatty acids such as C12:0, by paying a lower entropic cost upon receptor binding.

Structural comparison of $RpfR_{Ct}$(PAS)–C12:0 and $RpfR_{Ct}$(PAS)–BDSF reveals mostly subtle conformational changes localized to the $RpfR_{Ct}$(PAS) domain ligand-binding side chains (Fig 2B and 2E). One conformational difference is $RpfR_{Ct}$–R187, which makes an additional H-bond to the BDSF carboxylic acid than it makes to the C12:0 carboxylic acid (Fig 2B and 2E). Interestingly, $RpfR_{Ct}$–R187 can mediate this additional H-bond because it adopts a different rotameric configuration in the BDSF-bound structure. Much of the $RpfR_{Ct}$–R187 side chain is solvent exposed, and we speculate that it could play a role in regulating the activity of the receptor C-terminal enzymatic PDE domain upon BDSF binding.

Based on the measured distances and atom types (Fig 2B and 2E, S4 Fig), BDSF appears to be interacting with the conserved $RpfR_{Ct}$ amino acid Asn202. As an α,β-unsaturated carboxylic acid, BDSF contains an electron deficient C_β (C3). We propose that the more electron rich N202 amide nitrogen interacts with the electron deficient C_β of BDSF. This interaction cannot occur for the fully saturated C12:0 and would be significantly weaker for *trans*-2 dodecenonic acid because its C_β would be suboptimally positioned further away from N202. Additionally, in some RpfR proteins, there is a tyrosine corresponding to $RpfR_{Ct}$–Y183, whose hydroxyl interacts with the N202 side chain amide N-H (Fig 2E). This interaction could further increase the electron density on the N202 amide nitrogen, strengthening its interaction with C_β (C3) of BDSF.

Finally, it is important to note that due to the presence of the *cis*-2 or *trans*-2 double bond in BDSF and *trans*-2 dodecenoic acid, respectively, they are more rigid than their saturated isomer C12:0. Theoretically, there is less entropy lost upon receptor binding to BDSF or *trans*-2 dodecenoic acid than upon binding to C12:0. Thus, we speculate that in addition to the specific receptor contacts mediated by the BDSF *cis*-2 double bond, it could contribute to receptor affinity and specificity by lowering the entropic penalty paid in comparison to saturated fatty acids.

BDSF-mediated quorum sensing is regulated by an interaction between its receptor and synthase

We have discovered a previously unidentified PAS-like domain at the RpfR N-terminus and demonstrated that it binds directly to RpfF, inhibiting BDSF synthesis in vitro and in vivo (Fig

4B; Fig 6A and 6B), ultimately affecting the cellular concentration of c-di-GMP (Fig 6C). Ongoing studies in our labs are examining the molecular basis of this regulation. Due to the proximity of the RpfR FI domain to the RpfF substrate tunnel entrance (Fig 5C and 5D), in all likelihood, RpfR sterically blocks acyl-ACP binding to RpfF and acyl-ACP substrate access to the RpfF active site.

While we have shown that RpfR(FI) interacts with RpfF—tuning or restraining the amount of BDSF produced and secreted—we believe that RpfR(FI) has also evolved to limit the amount of general acyl-ACP substrate cleavage. It was previously demonstrated that RpfF cleaves a broad range of acyl-ACP substrates, producing free fatty acids, which is energetically wasteful, as many of these would not be DSF AI compounds or serve any other known physiological role [15,17,42, 43]. Many bacteria that express RpfF also contain an enzyme, regulation of pathogenicity factor B (RpfB), that salvages free fatty acids by ligating them to coenzyme A (CoA), generating substrates for beta oxidation [43]. RpfB was shown to be important for counteracting RpfF substrate promiscuity, as *rpfB* mutants displayed RpfF-dependent growth defects [43]. It is important to note that bacteria encoding RpfR do not contain RpfB, and how these bacteria might compensate for RpfF substrate cleavage promiscuity was unknown. We propose that an important role for RpfR(FI) is to compensate for the lack of RpfB in these bacteria by tightly regulating RpfF, governing its cleavage of acyl-ACP substrates.

Based on the existing data, we propose the following model for RpfR function (Fig 7). At low-cell density and below a critical concentration of BDSF, the RpfR c-di-GMP PDE has minimal activity [22], and biofilms can form because c-di-GMP levels are elevated. Why the RpfR PDE domain is minimally active in the absence of BDSF is unknown, but we hypothesize that the RpfR PAS domain may directly interact with the PDE domain inhibiting its activity. Throughout cellular growth, RpfR directly regulates RpfF processing of acyl-ACP substrates. More specifically, the newly discovered RpfR FI domain binds RpfF at its acyl-ACP–binding site, limiting its promiscuous cleavage of acyl-ACP substrates. Ultimately, the BDSF concentration reaches a critical concentration in which its binding to the RpfR PAS domain activates RpfR c-di-GMP PDE activity. This activation converts c-di-GMP to pGpG, triggering biofilm dispersal. It is important to note that PDE domains are typically allosterically activated upon dimerization [44–47]. We propose that BDSF binding to the RpfR PAS domain activates RpfR PDE activity by triggering RpfR dimerization or the conformational rearrangement of catalytically inactive (autoinhibited) RpfR dimers. In fact, a similar model was proposed for the regulator of biofilm dispersal of *Pseudomonas aeruginosa* (RbdA) [48]. Finally, what role, if any, BDSF binding to RpfR(PAS) plays in controlling the RpfR(FI)–RpfF association is unknown; however, if BDSF binding to RpfR(PAS) regulates RpfR(FI)–RpfF association, in turn controlling RpfF activity, then BDSF, RpfR, and RpfF comprise a feedback loop regulating BDSF synthesis. Determining whether such a feedback loop exists and elucidating the structural basis of its function is necessary if we are to understand the regulatory controls modulating BDSF synthesis and cell–cell communication.

Finally, we note that PAS and PAS-like domains structurally similar to the RpfR FI domain are common components of histidine kinases as well as other bacterial signal transduction proteins [23]. It will be interesting to determine whether some of these domains, like the FI domain, function to directly regulate the activity of a target enzyme. We propose that these interactions, like the physiologically important interactions identified here between RpfR and the AI BDSF as well as between RpfR and the BDSF synthase RpfF, could be targeted for the development of signaling agonists or antagonists and could serve as therapeutics modulating critical bacterial developmental processes including biofilm formation, biofilm dispersal, and virulence.

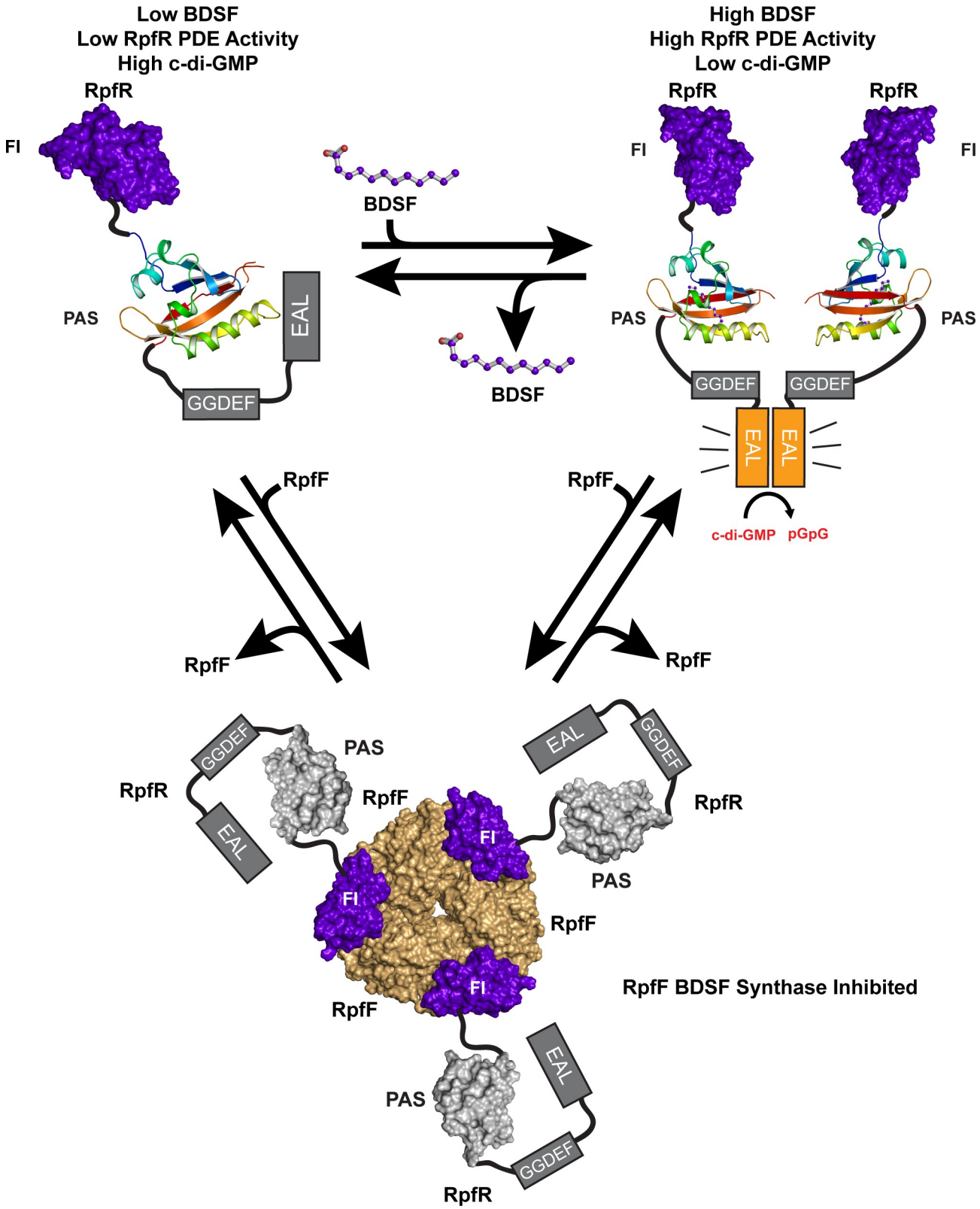

Fig 7. Proposed mechanism of RpfR activation by BDSF and RpfF inhibition by RpfR. At low-cell density (top left), BDSF levels are low and the RpfR PDE domain is minimally active, permitting elevated levels of c-di-GMP and favoring biofilm formation. Here, we depict a theoretical regulatory interaction between the PAS (rainbow cartoon) and PDE (gray box) domains. At high-cell density (top right), BDSF has accumulated and bound to the

RpfR PAS domain. This activates the RpfR PDE domain to degrade c-di-GMP to pGpG, favoring biofilm dispersal. Here, we depict RpfR PDE domain dimerization occurring upon BDSF binding; however, PDE activation may also occur via the rearrangement of catalytically inactive (autoinhibited) RpfR dimers. Throughout cellular growth, the RpfR FI domain (purple surface) associates with RpfF (light orange) (bottom), restraining BDSF synthesis, in turn modulating the cellular level of c-di-GMP. BDSF, *Burkholderia* DSF; c-di-GMP, bis-(3′-5′)-cyclic dimeric guanosine monophosphate; DSF, diffusible signal factor; FI, RpfF interaction; PAS, Per-Arnt-Sim; PDE, phosphodiesterase; pGpG, 5′-phosphoguanylyl-(3′,5′)-guanosine; RpfF, regulation of pathogenicity factor F; RpfR, regulation of pathogenicity factor R.

https://doi.org/10.1371/journal.pbio.3000123.g007

Materials and methods

Protein production for X-ray crystallography

$RpfR_{Ct}$(FI). *$rpfR_{Ct}$*(FI) (amino acids 1–95) was PCR amplified from synthetic full-length *C. turicensis* z3032 *rpfR* (codon optimized for *E. coli* expression, Genscript) using Phusion High-Fidelity DNA Polymerase (New England Biolabs) and the oligonucleotide pair primer 1 and primer 2. The amplified insert was analyzed using a 0.1% agarose gel, and the band corresponding to the insert was excised and gel purified. Gibson Assembly (New England Biolabs) was used to integrate the purified insert into pTB146 [49] and linearized using the restriction enzymes SapI and XhoI to generate the vector pHis6-SUMO-$RpfR_{Ct}$(FI).

pHis6-SUMO-$RpfR_{Ct}$(FI) was transformed and overexpressed in *E. coli strain* BL21(DE3) by growing cells at 37 ˚C and 200 RPM in LB medium containing 100 μM ampicillin until OD_{600} = 0.9. Cells were induced using 500 μM isopropyl β-D-1-thiogalactopyranoside (IPTG) and grown for a further 20 h at 18 ˚C and 200 RPM. Cells were then pelleted at 7,000 × g for a period of 15 min.

Pelleted cells were resuspended in buffer A (500 mM NaCl, 50 mM HEPES [pH 7.5], 40 mM imidazole, 10 μg/mL DNAse, and 1 mM phenylmethanesulfonyl fluoride [PMSF]). The cells were lysed by two passages through a cell disruptor, and the cell lysate was subsequently clarified at 35,000 × g for a period of 45 min at 4 ˚C. Clarified lysate was passed over His60 Superflow Ni Resin (Takara Bio, United States of America) equilibrated in buffer A. The resin was washed with buffer A and was eluted with an increasing step gradient of imidazole in buffer A. Fractional purity was evaluated using SDS-PAGE. The highest purity fractions were pooled and dialyzed overnight against buffer B (100 mM NaCl, 50 mM HEPES [pH 7.5]). His_6-Ulp1 SUMO protease was added to the pooled fractions prior to dialysis to cleave the His_6-SUMO affinity tag.

Following cleavage, the dialyzed sample was reapplied to fresh His60 Superflow resin to remove the majority of the His_6-SUMO tag and His_6-Ulp1, with the flow-through containing $RpfR_{Ct}$(FI). The flow-through was subsequently diluted using buffer C (50 mM HEPES [pH 7.5]) to a final concentration of 50 mM NaCl and 50 mM HEPES (pH 7.5). The diluted protein was then passed over a MonoQ anion exchange column (GE Healthcare). $RpfR_{ct}$(FI) eluted in the MonoQ column flow-through and was separated from all significant contaminants. Following anion exchange, the pure fractions of $RpfR_{Ct}$(FI) were pooled and concentrated using a 3-kDa molecular weight–cutoff pressure concentrator (Sartorius) and loaded onto a Superdex 200 16/70 column (GE Healthcare) equilibrated with buffer D (100 mM NaCl, 20 mM MOPS [pH 7.0], and 1 mM TCEP). Following size exclusion chromatography, $RpfR_{ct}$(FI) was concentrated to 7.9 mg/mL (A_{280} 0.1% [= 1 g/L] = 1.353, calculated using the ExPASy ProtParam server [50]) using a 3-kDa cutoff Vivaspin concentrator and stored at −80 ˚C.

Selenomethionyl (SeMet) $RpfR_{Ct}$(FI) was produced by following a modified version of a published protocol for incorporating selenomethionine into proteins [51]. BL21(DE3) cells were transformed with pHis6-SUMO-$RpfR_{Ct}$(FI) and grown in minimal media containing 100 μM ampicillin at 37 ˚C and 200 RPM until OD_{600} = 0.76. Using sterile technique, the cells were pelleted at 3,000 RPM for 15 min, and the minimal media supernatant was removed.

Cells were washed twice with a buffer containing 10 g/L K_2HPO_4 and 1 g/L sodium acetate. Cells were then resuspended in fresh minimal media containing 100 μM ampicillin and 50 mg/L selenomethionine in place of methionine. Cells were induced with 500 μM IPTG and grown for an additional 15.5 h at 18 ˚C and 200 RPM. Cells were pelleted at 7,000 × g for 15 min. The purification of SeMet $RpfR_{Ct}$(FI) was identical to that of native protein.

$RpfR_{Ct}$(FI)–$RpfF_{Bc}$. Full-length *$rpfF_{Bc}$* (amino acids 1–287) was amplified using Phusion High-Fidelity DNA Polymerase and WT *B*. *cenocepacia* HI2424 genomic DNA with the oligonucleotide pair primer 3 and primer 4. The gel purified insert was cloned into pBB75 that had been linearized using NdeI and EcoRI. Gibson Assembly was then used to generate the construct, $pRpfF_{Bc}$.

pHis6-SUMO-$RpfR_{Ct}$(FI) and $pRpfF_{Bc}$ were cotransformed into BL21(DE3) cells and grown to OD_{600} = 0.9 at 37 ˚C and 200 RPM in LB medium containing 100 μM ampicillin and 30 μM kanamycin, after which expression of both proteins was induced by the addition of 500 μM IPTG. Following induction, cells were grown for an additional 11 h at 25 ˚C and 200 RPM and pelleted by centrifugation at 7,000 × g for 15 min.

Cells were resuspended in buffer E (300 mM NaCl, 50 mM HEPES [pH 8.0], 20 mM imidazole, 5% [vol/vol] glycerol, 10 μg/mL DNAse, and 1 mM PMSF) and lysed by two passages through a French press at approximately 25,000 PSI. Lysate was clarified at 35,000 × g for 45 min at 4 ˚C. Clarified lysate was applied to His60 Superflow resin equilibrated with buffer E. The resin was then washed with buffer E containing 40 mM imidazole. His_6-SUMO-$RpfR_{ct}$(FI) coeluted in a 1:1 stoichiometric amount with $RpfF_{Bc}$ following an increasing step gradient of imidazole in buffer E. Fractional purity was evaluated by SDS-PAGE, and the highest purity fractions were combined and dialyzed overnight against buffer F (100 mM NaCl, 50 mM HEPES [pH 8.0], and 5% [vol/vol] glycerol) in the presence of His_6-Ulp1 SUMO protease. The His_6-SUMO tag and His_6-Ulp1 were subsequently removed by passing the dialyzed sample over fresh His60 Superflow resin equilibrated with buffer F. Pure $RpfR_{Ct}$(FI)–$RpfF_{Bc}$ complex was concentrated using a 10-kDa cutoff filter (Sartorius) and loaded onto a Superdex 200 16/70 column equilibrated with buffer G (100 mM NaCl, 20 mM HEPES [pH 8.0], 1% [vol/vol] glycerol, and 1 mM TCEP). Fractions of the complex were subsequently combined and concentrated to 3.35 mg/mL (as evaluated by the Bradford method) using a 10-kDa cutoff Vivaspin concentrator.

$RpfR_{Ct}$(PAS). *$rpfR_{Ct}$*(PAS) (amino acids 115–224) was PCR amplified from synthetic full-length *C*. *turicensis* z3032 *rpfR* using Phusion High-Fidelity DNA Polymerase and the oligonucleotide pair primer 5 and primer 6. Gibson Assembly was used to insert the gel purified insert into XhoI/SapI linearized pTB146, generating vector pHis6-SUMO-$RpfR_{Ct}$(PAS). His_6-SUMO-$RpfR_{Ct}$(PAS) was overexpressed in BL21(DE3) cells transformed with pHis6-SUMO-$RpfR_{Ct}$(PAS) grown to OD_{600} = 0.60 at 37 ˚C and 220 RPM and then moved to 18˚ C and 200 RPM. When the OD_{600} reached 0.90, expression was induced with 500 μM IPTG, and cells were grown for an additional 18 h at 18 ˚C and 200 RPM. Following induction, cells were harvested by pelleting at 7,000 × g for 15 min.

Cell pellets were resuspended in buffer H (1 M NaCl, 50 mM HEPES [pH 7.0], 20 mM imidazole, 10 μg/mL DNAse, and 1 mM PMSF). Cells were lysed following two passages through a cell disruptor, and the lysate was clarified at 35,000 × g for a period of 45 min at 4 ˚C. The lysate was passed over His60 Superflow Ni resin equilibrated in buffer H and was washed using buffer H. $RpfR_{Ct}$(PAS) was eluted using buffer H containing increasing concentrations of imidazole. Fractional purity was assessed using SDS-PAGE. The highest purity fractions were pooled and combined with His_6-Ulp1 SUMO protease. The protease reaction was dialyzed overnight against buffer H absent imidazole. The dialyzed fraction was passed over fresh His60 Superflow resin to remove His_6-Ulp1 and the His_6-SUMO tag. The pure

$RpfR_{Ct}$(PAS) in the flow-through was subsequently concentrated using a 3-kDa Vivaspin cut-off filter and loaded onto a Superdex 200 16/70 column equilibrated with buffer I (100 mM NaCl, 20 mM HEPES [pH 7.0], and 1 mM TCEP). Following size exclusion chromatography, $RpfR_{ct}$(PAS) was concentrated to 4.7 mg/mL (as evaluated by the Bradford method) using a 3-kDa cutoff Vivaspin concentrator and stored at −80 ˚C.

The $RpfR_{ct}$(PAS)–BDSF complex was obtained by coexpressing His_6-SUMO-$RpfR_{Ct}$(PAS) and full-length $RpfF_{Bc}$ (amino acids 1–287) using BL21(DE3) cells cotransformed with plasmids pHis6-SUMO-$RpfR_{Ct}$(PAS) and $pRpfF_{Bc}$. Cells were grown at 37 ˚C and 220 RPM in LB medium containing 100 μM ampicillin and 30 μM kanamycin until OD_{600} = 0.9. The temperature was then decreased to 18 ˚C and expression was induced with 100 μM IPTG. Cells were grown for an additional 16 h prior to harvesting. All subsequent purification steps of the $RpfR_{Ct}$(PAS)–BDSF complex were identical to the purification of the $RpfR_{Ct}$(PAS)–C12:0 complex, as described above.

Crystallization and diffraction data collection

$RpfR_{Ct}$(FI). Crystals of $RpfR_{Ct}$(FI) were obtained by the hanging drop vapor diffusion method at 20 ˚C. A 1:1 mixture of protein solution (7.9 mg/mL $RpfR_{Ct}$[FI], 1 mM BDSF, and 0.62% [vol/vol] DMSO) and mother liquor solution (75 mM NaH_2PO_4 and 20% [vol/vol] PEG 3350) was set up above a well containing 700 μL mother liquor solution. Crystals appeared overnight and were cryoprotected by soaking into a solution of 75 mM NaH_2PO_4, 20% (vol/vol) PEG 3350, 15% (vol/vol) glycerol, 1 mM BDSF, and 0.62% (vol/vol) DMSO. Crystals grew in the presence or absence of 1 mM BDSF (Sigma-Aldrich) and 0.62% (vol/vol) DMSO. SeMet derived crystals were obtained by mixing SeMet-$RpfR_{Ct}$(FI) (6.7 mg/mL) with mother liquor solution (100 mM NaH_2PO_4 and 17.5% [vol/vol] PEG 3350) in a 1:1 ratio over a well containing 700 μL mother liquor solution. Crystals were cryoprotected using 100 mM NaH_2PO_4, 17.5% (vol/vol) PEG 3350, and 15% (vol/vol) glycerol.

Data were collected at the Stanford Synchrotron Radiation Lightsource (SSRL) beamline 14–1 using a MARmosaic 325 CCD detector and processed using the HKL software package [52]. Initial phases were calculated with the SAD method using PHENIX (AutoSol) [53]. AutoSol located the position of the individual Se atoms and built an initial mode to 1.1 Å resolution with a 0.554 figure of merit. PHENIX(AutoBuild) [54] was used to further build and refine the model, followed by subsequent manual model building in COOT [55] and refinement using PHENIX [56]. The completed SeMet model was refined into data collected from an isomorphic native crystal of $RpfR_{Ct}$(FI) to a resolution of 1.2 Å. Early rounds of refinement included simulated annealing, individual B-factors, real space, rigid body, and individual atomic coordinate refinement. In later rounds, waters and hydrogens were included, and ADP weighting was optimized.

$RpfR_{Ct}$(PAS)–C12:0. Crystals of $RpfR_{Ct}$(PAS) bound to lauric acid were grown using the sitting drop vapor diffusion method at 20 ˚C. An $RpfR_{Ct}$(PAS) protein solution (4.7 mg/mL $RpfR_{Ct}$[PAS],1 mM BDSF, and 0.62% [vol/vol] DMSO) was combined 1:1 with the mother liquor solution (200 mM sodium formate, 18% [vol/vol] PEG 3350, and 100 mM HEPES [pH 7.75]) and allowed to equilibrate above a well containing 700 μL mother liquor solution. Crystals were cryoprotected in a solution containing 200 mM sodium formate, 20% (vol/vol) PEG 3350, 100 mM HEPES (pH 7.75), 1 mM BDSF, 0.62% (vol/vol) DMSO, and 15% (vol/vol) glycerol. Data were collected at SSRL beamline 9–2 using a Dectris Pilatus 6M detector and processed using the HKL software package [52].

Initial phases for $RpfR_{Ct}$(PAS)-lauric acid were determined in Phaser [57] using the molecular replacement method and the N-terminal PAS domain of PpANR MAP3K from

Physcomitrella patens (PDB:5IU1) [58] as a search model. The initial model building and refinement were performed using PHENIX (AutoBuild) [54] with three rounds of simulated annealing to remove phase bias from the starting model. Further manual building was performed using COOT [55] and refined in PHENIX [56]. Individual atomic coordinates, real-space, and individual B-factors were refined during the early stages of model building. As the model improved, excess difference density that did not resemble water or sidechain density became prominent. C12:0 was successfully built into the excess difference density. During the final stages of refinement, TLS parameters (generated in PHENIX [59]) and ADP-optimized weights were included in the refinement, and hydrogens were added to the model. While some electron density corresponding to residues 115 and 207–212 was evident, attempts to build and refine residues into this disordered region of the map were unsuccessful.

$RpfR_{Ct}$(PAS)–BDSF. Crystals of $RpfR_{Ct}$(PAS)–BDSF were produced by the hanging drop vapor diffusion method at 20 ˚C by mixing $RpfR_{Ct}$(PAS)–BDSF (4.7 mg/mL) with mother liquor solution (150 mM lithium citrate and 16% [vol/vol] PEG 3350) in a 1:1 ratio above a well containing 700 μL mother liquor solution. Crystals were cryoprotected by soaking in 150 mM lithium citrate, 16% (vol/vol) PEG 3350, and 15% (vol/vol) glycerol.

Data were collected on a home source Rigaku Micro/Max-007HF Rotating Copper Anode X-ray Generator using a Rigagku RAXIS-IV++ detector and processed with the HKL software package [52]. Phaser [57] was used to obtain initial phases of $RpfR_{Ct}$(PAS)–BDSF by using the previously determined structure of $RpfR_{Ct}$(PAS)–C12:0 (PDB:6DGG) as a search model. In order to reduce the effect of phase bias on ligand density, C12:0 and all water molecules were removed from the search model, and three rounds of simulated annealing were performed during the initial stages of refinement to remove any phase bias toward ligand identity. Individual atomic coordinates, real-space, rigid body, and individual B-factors were initially refined, with TLS parameters (generated in PHENIX [59]) and individual ADP weights added during later rounds of refinement. Midway through refinement, both C12:0 and BDSF were built into the model and refined separately. BDSF and its accompanying restraints were generated using PHENIX (eLBOW) [60] and assigned the three letter code GEY. While both ligands fit the difference density in the $RpfR_{Ct}$(PAS) ligand-binding pocket, C12:0 adopted the synperiplanar configuration of BDSF following refinement. BDSF was included in the model for the duration of the refinement. Near the end of the refinement, hydrogens were included in the model. Insufficient electron density was available to build the following residues: 115 and 206–212. As with the C12:0 complexed structure, while electron density was present for residues 206–212, all attempts to build productively into the density were unsuccessful.

$RpfF_{Bc}$–$RpfR_{Ct}$(FI). Crystals of the $RpfF_{Bc}$–$RpfR_{Ct}$(FI) complex were grown using the hanging drop vapor diffusion method at 20 ˚C by mixing $RpfF_{Bc}$–$RpfR_{Ct}$(FI) (3.35mg/mL) with mother liquor solution (100 mM sodium acetate [pH 5.6] and 250 mM ammonium phosphate dibasic) in a 1:2 ratio above a well containing 700 μL mother liquor solution. Crystals were cryoprotected by soaking in a solution of 100 mM sodium acetate (pH 5.6), 250 mM ammonium phosphate dibasic, and 30% (vol/vol) glycerol. Data were collected at SSRL beamline 9–2 using a Dectris Pilatus 6M detector and processed using the HKL software package [52].

Initial phases were obtained by molecular replacement using Phaser [57], with the structures of $RpfR_{Ct}$(FI) (PDB:6DGA) and *B. cenocepacia* RpfF (PDB:5FUS) as search models [17]. In the early stages of model building, simulated annealing, rigid-body, individual atomic coordinates, individual B-factors, and real-space refinement were performed in PHENIX [56]. As refinement proceeded, rigid-body refinement and simulated annealing were discontinued, while TLS parameters (generated in PHENIX [59]), ADP-optimized weights, and waters were included. There was insufficient electron density to build the following residues: $RpfF_{Bc}$ 1,

278–287, and $RpfR_{Ct}$(FI) 1–4. During the later stages of refinement, hydrogens were added to the model. Additionally, four molecules of glycerol and one molecule of phosphate were built into their corresponding electron density.

Protein production for RpfR(FI)–RpfF enzymatic assay

AasS. *V. harveyi aasS*, codon optimized for expression in *E. coli*, was synthesized and inserted into pET15-b expression vector containing an amino-terminal His_6-tag to create pAasS (Genscript). Following methods previously described [61,62], pAasS was transformed into chemically competent BL21(DE3) cells and grown to OD_{600} = 0.6 at 37 ˚C and 200 RPM in LB medium containing 100 μM ampicillin, at which point the cells were moved to 25 ˚C and 200 RPMS and induced using 1 mM IPTG when they reached OD_{600} = 0.9. Cells were further grown for an additional 20 h and harvested following centrifugation at 7,000 × g for 15 min.

The cell pellet was resuspended in Buffer J (300 mM NaCl, 20 mM Tris-HCl [pH 7.5], 10% [vol/vol] glycerol, and 10 mM imidazole) and lysed by two passes through a French press at approximately 25,000 PSI. Cell lysate was clarified at 35,000 × g at 4 ˚C for 40 min. Clarified lysate was applied to His60 Superflow resin equilibrated with Buffer J. The resin was washed with Buffer J containing 40 mM imidazole. His_6-AasS was eluted using an increasing gradient of imidazole in Buffer J and analyzed using SDS-PAGE. The purest fractions were combined and dialyzed into the final AasS storage buffer, Buffer K (20 mM Tris [pH 7.5], 10% [vol/vol] glycerol, 1 mM EDTA, 0.1 mM DTT, and 0.002% [vol/vol] Triton X-100). Dialyzed AasS was concentrated to 3.07 mg/mL (A_{280} 0.1% [= 1 g/L] = 1.05 calculated with the ExPASy ProtParam server [50]), with a 30-kDa cutoff Vivaspin concentrator and stored at −80 ˚C.

$RpfR_{Bc}$(FI). *B. cenocepacia rpfr$_{Bc}$(FI)* (amino acids 1–94) was amplified using Phusion High-Fidelity DNA Polymerase from WT *B. cenocepacia* HI2424 genomic DNA and the oligonucleotide pair primer 7 and primer 8. The PCR amplified insert was gel purified and cloned into a SapI/XhoI linearized pTB146 vector using the Gibson Assembly to generate pHis6-SUMO-$RpfR_{Bc}$(FI).

pHis6-SUMO-$RpfR_{Bc}$(FI) was transformed into BL21(DE3) cells and grown to OD_{600} = 0.70 in LB containing 100 μM ampicillin at 37 ˚C and 200 RPM then moved to 18 ˚C and 200 RPM. Upon reaching OD_{600} = 0.9, expression was induced with 500 μM IPTG. Cells were grown for an additional 17 h at 18 ˚C and 200 RPM and harvested by centrifugation at 7,000 × g for 15 min. $RpfR_{Bc}$(FI) was purified identically to $RpfR_{Ct}$(FI) (see above) and concentrated to a 549 μM (extinction coefficient = 11,000 M^{-1} cm^{-1} calculated with the ExPASy ProtParam server [50]).

$RpfF_{Bc}$. Full-length *rpfF$_{Bc}$* (amino acids 1–287) was amplified with Phusion High-Fidelity DNA Polymerase from WT *B. cenoecacia* HI2424 genomic DNA and the oligonucleotide pair primer 9 and primer 10. The PCR insert was gel purified and cloned into a SapI/XhoI linearized pTB146 vector using the Gibson Assembly to generate pHis6-SUMO-$RpfF_{Bc}$. pHis6-SUMO-$RpfF_{Bc}$ was transformed into BL21(DE3) cells and grown in LB medium containing 100 μM ampicillin and supplemented with 0.2% (vol/vol) glucose. Cells were grown to an OD_{600} = 0.78 at 37 ˚C and 220 RPM. Cells were then moved to 25 ˚C and 200 RPM and induced with 500 μM IPTG upon reaching OD_{600} = 0.93. Following induction, cells were grown for an additional 20 h and harvested by pelleting at 7,000 × g for 10 min.

His_6-SUMO-$RpfF_{Bc}$ was purified using a protocol similar to that previously reported [17], with the following modifications. Cells were resuspended in buffer L (300 mM NaCl, 50 mM Na phosphate [pH 8.0], 5% [vol/vol] glycerol, 10 mM imidazole, and 10 μg/mL DNAse) and passed two times through a cell disruptor. Lysate was clarified at 35,000 × g for 40 min at 4 ˚C.

Clarified cell lysate was incubated overnight with gentle rocking in the presence of His60 Superflow resin equilibrated in buffer L at 4 ˚C. The resin was packed into a column and washed using 40 mM imidazole in buffer L. His_6-SUMO-$RpfF_{Bc}$ was eluted from the resin using a step gradient of 100, 250, and 500 mM imidazole in buffer L. The purest fractions were combined and dialyzed overnight in the presence of His_6-Ulp1 SUMO protease into buffer M (100 mM NaCl, 50 mM Na phosphate [pH 8.0], and 5% [vol/vol] glycerol) to remove imidazole. The dialyzed protein was incubated with fresh His60 Superflow resin for 1 h at 4 ˚C with gentle rocking to remove the His_6-SUMO tag and His_6-Ulp1. The pure $RpfF_{Bc}$ that flowed through the column was concentrated using a 10-kDa cutoff pressure concentrator to 1.71 mg/mL (evaluated using the Bradford method) and loaded onto a Superdex 200 16/70 column equilibrated with buffer N (100 mM NaCl, 50 mM Na phosphate [pH 8.0], 5% [vol/vol] glycerol, and 1 mM TCEP). Peak fractions were analyzed with SDS-PAGE and combined to a final concentration of 6.4 μM (extinction coefficient = 36,900 M^{-1} cm^{-1} calculated with the ExPASy ProtParam server [50]). Aliquots of $RpfF_{Bc}$ were stored at −80 ˚C.

acpP and *acpS* cloning

Obtaining holo-ACP_{Ec} (ACP_{Ec} with the 4′-phosphopantetheinyl prosthetic group on serine 36) requires ACP to be coexpressed alongside the *E. coli* Acyl Carrier Protein Synthase ($AcpS_{Ec}$). To coexpress ACP_{Ec} and $AcpS_{Ec,}$ we engineered a construct similar to the one previously described in [63], by cloning $acpP_{Ec}$ and $acpS_{Ec}$ into pQlink-H and pQlink-N, respectively [64]. pQlink-H was chosen in order to facilitate ACP_{Ec} purification using a TEV protease cleavable His_7-tag. Both inserts were amplified from *E. coli MG1655* genomic DNA using Phusion High-Fidelity DNA Polymerase. The $acpP_{Ec}$ insert was generated using the oligonucleotide pair primer 11 and primer 12. The $acpS_{Ec}$ insert was amplified using the oligonucleotide pair primer 13 and primer 14. Amplified and gel purified $acpP_{Ec}$ was inserted into BamHI and NotI linearized pQlink-H using the Gibson Assembly to generate plasmid pAcpP_{Ec}-His7. Likewise, amplified and gel purified $acpS_{Ec}$ was inserted into BamHI and NotI linearized pQlink-N, generating pAcpS_{Ec}.

A single-expression construct for both proteins was generated by digesting pAcpS_{Ec} with PacI and pAcpP_{Ec}-His7 with SwaI. Following heat inactivation of the restriction digests at 65 ˚C for 20 min, both reactions were incubated with LIC-qualified T4 DNA polymerase (Novagen) in the presence of either dCTP (pAcpS_{Ec} digest) or dGTP (pAcpP_{Ec}-His7 digest) at 25 ˚C for 30 min. The T4-treated DNA fragments were then combined in a 1:1 ratio and annealed at 65 ˚C for five min, followed by a 2 min incubation on ice and a 15 min incubation at room temperature. Following the addition of EDTA to a final concentration of 1.25 mM, the annealing reactions were transformed into Lucigen SOLO hypercompetent cells (Lucigen), generating pHis7-AcpP_{Ec}/N-AcpS_{Ec}.

Holo-ACP purification

Purification of holo-ACP_{Ec} was accomplished using several modified protocols [62,63,65]. pHis7-AcpP_{Ec}/N-AcpS_{Ec} was transformed into C41(DE3) chemically competent *E. coli* cells and grown up in LB medium containing 100 μM ampicillin. Cells were grown to OD_{600} = 0.6 at 37 ˚C and 220 RPM and induced with 1 mM IPTG. Following induction, cells were grown for an additional 22 h at 18 ˚C and 200 RPM and then pelleted at 7,000 × g for 15 min. The pellet was resuspended in lysis buffer O (500 mM NaCl, 50 mM Tris [pH 8.8], 10 mM $MgCl_2$, 5 mM β-mercaptoethanol, 20 mM imidazole, and 10 μg/mL DNAse). Cells were lysed by two passages through a cell disruptor and clarified at 35,000 × g for 40 min at 4 ˚C. Clarified lysate was incubated with His60 Superflow resin equilibrated in buffer O for 1.5 h with gentle

rocking at 4 ˚C. The resin was washed once with buffer O and a second time with buffer O containing 40 mM imidazole. His_7-ACP_{Ec} copurified with $AcpS_{Ec}$ following elution with increasing concentrations of imidazole in buffer O. Fractional purity was analyzed with SDS-PAGE. The purest fractions were combined with His_6-TEV protease. EDTA was added to a final concentration of 50 mM, and the reaction was incubated at 4 ˚C overnight. The overnight reaction was then dialyzed against buffer P (50 mM NaCl, 25 mM MOPS [pH 7.1], and 1mM β-mercaptoethanol) to remove imidazole. Dialyzed fractions were incubated with fresh His60 Superflow resin equilibrated in buffer P and allowed to rock at 4 ˚C for 2 h to remove the His_7-tag and His_6-TEV protease. The flow-through from the resin was loaded onto a Q Sepherase Fast Flow Column (Pharmacia) equilibrated in buffer P. Holo-ACP_{Ec} was successfully separate from $AcpS_{Ec}$ using an increasing gradient of KCl in buffer P. The purest holo-ACP_{Ec} fractions were combined and concentrated using a 3-kDa cutoff filter and loaded onto a Superdex 200 16/70 column equilibrated in buffer Q (100 mM NaCl, 20 mM Tris [pH 7.5], and 0.87 mM TCEP). Peak fractions were analyzed using SDS-PAGE and concentrated to 444.4 μM (extinction coefficient = 1,800 M^{-1} cm^{-1} [Sigma-Aldrich]) using a 3-kDa Vivaspin concentrator.

ACP-charging reaction

Optimal charging reaction conditions were based on those previously reported [15,16,63]. C12:0–ACP_{Ec} was charged with substrate by incubating 142 μM holo-ACP_{Ec} with 2.5 mM C12:0, 10 mM ATP, 2 μM AasS, in ACP-charging buffer R (100 mM Tris [pH 7.8], 10 mM $MgCl_2$, and 1 mM TCEP) for 4 h at 37 ˚C. Following charging, the reaction was precipitated by the addition of two equivalent reaction volumes of acetone and incubated at −20 ˚C overnight. The precipitated protein was pelleted at 20,000 × g for 30 min. The supernatant was removed, and the pellet was washed two times with two additional reaction volumes of acetone. The pellet was then air dried and dissolved in 20 mM Tris (pH 7.5) to a final concentration of 111 μM charged-ACP_{Ec}.

RpfF thioesterase assay

The thioesterase reaction conditions were chosen based on previously published methodologies [15,16]. RpfF thioesterase activity was measured using a 10-μL reaction consisting of 78 μM C12:0–ACP_{Ec} substrate, 0.64 μM $RpfF_{Bc}$ (or control buffer N), and either 6.4 μM $RpfR_{Bc}$(FI), 1.28 μM $RpfR_{Bc}$(FI), or control buffer D in the thioesterase assay buffer (100 mM Tris [pH 7.5]). This reaction was incubated at 37 ˚C for 30 min and then heat inactivated at 95 ˚C for 2 min. Reactions were analyzed with a conformation-sensitive nondenaturing gel containing 20% polyacrylamide, 375 mM Tris (pH 8.8), and 2.5 M urea. Gels were stained with Coomassie Brilliant Blue, and band intensities were measured using a LI-COR Odyssey CLx Imager System (LI-COR Biosciences) and quantified using Image Studio version 3.1 (LI-COR Biosciences).

Production of $RpfR_{Bc}$(FI-PAS)–$RpfF_{Bc}$. *B. cenocepacia* $rpfr_{Bc}$(FI-PAS) (amino acids 1–223) was amplified with Phusion High-Fidelity DNA Polymerase from WT *B. cenoecacia* HI2424 genomic DNA and the oligonucleotide pair primer 7 and primer 15. The PCR-amplified insert was gel purified and cloned into a SapI/XhoI linearized pTB146 vector using the In-Fusion method (Clonetech) to generate pHis6-SUMO-$RpfR_{Bc}$(FI-PAS).

pHis6-SUMO-$RpfR_{Bc}$(FI-PAS) and $pRpfF_{Bc}$ were cotransformed into BL21(DE3) cells and grown at 37 ˚C and 200 RPM to OD_{600} = 0.7 in LB medium containing 100 μM ampicillin and 30 μM kanamycin. At this point, the growth temperature was decreased to 25 ˚C. Upon reaching OD_{600} = 0.9, expression of both proteins was induced by the addition of 500 μM IPTG.

Following induction, cells were grown for an additional 17 h at 25 ˚C and 200 RPM and pelleted by centrifugation at 7,000 × g for 15 min.

Cells were resuspended in buffer S (300 mM NaCl, 50 mM HEPES [pH 8.0], 20 mM imidazole, 10% [vol/vol] glycerol, 10 μg/mL DNAse, and 1 mM PMSF) and lysed by two passages through a French press at approximately 25,000 PSI. Lysate was clarified at 35,000 × g for 45 min at 4 ˚C. Clarified lysate was applied to His60 Superflow resin equilibrated with buffer S. The resin was then washed with buffer S containing 40 mM imidazole. His_6-SUMO-$RpfR_{Bc}$(-FI-PAS) coeluted in a 1:1 stoichiometric amount with $RpfF_{Bc}$ following an increasing step gradient of imidazole in buffer S.

Genetic engineering of *B. cenocepacia*

Isogenic mutations were created using methods described by Fazli and colleagues [66]. For single-gene deletions, approximately 1,000 bp upstream and downstream of the target gene were amplified using high-fidelity PCR and joined using single overlap extension PCR, using the following conditions: 98 ˚C for 2 min; 3 cycles of 98 ˚C for 15 s, 64 ˚C for 30 s, 72 ˚C for 1 min; 72 ˚C for 1 min. After the addition of standard attB1 and attB2 primers, a second round of PCR was performed, using the following conditions: 98 ˚C for 2 min; 27 cycles of 98 ˚C for 15 s, 64 ˚C for 30 s, 72 ˚C for 2 min; 72 ˚C for 7 min. This approximately 2,000 bp fragment was then gel purified and inserted into a pDONPREX18Tp-SceI-PheS plasmid containing a trimethoprim (Tp) resistance cassette using Gateway cloning. For single-nucleotide mutations, the target gene was cloned into the same plasmid and site-directed mutagenesis was used to create the intended point mutation. The resulting gene-replacement vectors were electroporated into competent DH5α *E. coli* and introduced by conjugation into *B. cenocepacia* via triparental mating. Matings were performed by combining 200 μL of overnight cultures of the DH5α strain containing the gene replacement vector, 200 μL of S.17 *E. coli* containing the conjugation helper vector pEVS104, and 50 μL of the recipient *B. cenocepacia* strain into a cell pellet, resuspending the pellet in 30 μL of 10 mM $MgSO_4$ and spotting onto tryptic soy agar (TSA) plates. The cell mixture was scraped from the plate after 24 h at 37 ˚C using an inoculating loop, resuspended in 1 mL of PBS, and plated at different dilutions onto Vogel–Bonner minimal medium (VBMM) agar containing 100 μg/mL Tp. Four Tp-resistant colonies were selected and grown first in tryptic soy broth, followed by VBMM broth containing 0.1% chlorophenylalanine before being plated onto four TSA plates. 100 colonies from each plate were picked using pipette tips and patched onto both TSA and TSA-Tp100. Four candidates for each mutation were selected by sensitivity to Tp and sequenced using whole genome sequencing according to Baym and colleagues [67] on an Illumina NextSeq 500 to a minimum average of 30x coverage. The correctly made mutants were confirmed to be otherwise isogenic using the variant calling program Breseq v. 0.31 [68].

Quantification of fitness in the biofilm life cycle

Freezer stocks were revived overnight and then grown for 24 h in M9 minimal medium + 3% galactose (GMM) at 37 ˚C. Equal volumes of each competitor were added to 3% GMM containing three 7 mm polystyrene beads, and a planktonic sample of that mixture was serially diluted and plated on half-strength T-soy X-gal plates to enumerate starting CFU/mL. Samples taken from a bead at subsequent 12-h time intervals over 48 total h were serially diluted and plated in half-strength T-soy X-gal plates to enumerate CFU/bead. Fitness was calculated as the difference in Malthusian parameters between the mutant and wild type ancestor in units of $time^{-1}$, as follows: $\ln(Nm1/Nm0) - \ln(N_{WT}1/N_{WT}0)$, in which N is cell number and m is

mutant and WT is wild type at time 0 or 1 (e.g., *Nm*1 is the number of mutant cells at time 1) [69].

Quantification of BDSF in *B. cenocepacia* supernatants

Four independent cultures of each strain (WT, Δ*rpfR*, Δ*rpfF*, and Δ*FI*) were inoculated into 2 mL Luria broth (LB) in test tubes from frozen stocks and grown at 35 ˚C, 200 RPM overnight (approximately 14 h). The next day, cultures were diluted 1:500 into 10 mL fresh LB in 50 mL flasks in quadruplicate and grown at 35 ˚C, 200 RPM for 12 h. After growth, 1 mL of culture was removed from each flask and placed into 2 mL tubes and 20 μL of culture was used to measure cell density by dilution plating. The cultures were centrifuged at max speed (15,000 × g) at room temperature for 1 min. Supernatants were removed and placed into new 2-mL tubes, and the solutions were acidified using 12 M HCl until the pH was less than 4.0. Three hundred μL of ethyl acetate was added to each sample, and the tubes were vortexed for 5 min. The samples were then centrifuged for 10 min at 8,000 × g at room temperature to separate organic and aqueous phases. The top (organic) phase was removed and placed into new 1.5-mL tubes. The resulting organic solution was evaporated using a heated vacuum centrifuge, and the dried pellet was resuspended in 100 μL 1:1 methanol/water, placed in mass spectrometry vials, and analyzed by liquid chromatography-mass spectrometry on a Xevo TQ-D Triple Quadruple mass spectrometer (Waters) coupled with an UPLC system (Acquity, model BSM).

Liquid chromatography separation was carried out on an Acquity UPLC BEH reverse-phase column (1.7 μm, 2.1 mm × 150 mm, Waters). Solvent A was 10 mM ammonium formate in water. Solvent B was 100% methanol. 10 μL of sample was autoinjected into the column and subjected to solvent A and B gradients as follows: t = 0 minutes, 10% solvent B; t = 4 minutes, 98% solvent B; t = 7.01 minutes, 10% solvent B at a flow rate of .200 mL/min for a total of 10 min per sample. Under these conditions, BDSF had a retention time of 5.6 min. BDSF was detected in selected reaction monitoring (SRM) in negative ionization mode following the *m/z* 198 → 197 at 30 eV. The signal for BDSF in biological samples was defined as the observed peak area on the chromatography trace determined by the MassLynx software (Waters). Chemically synthesized BDSF (Adipogen, San Diego, CA) was used to determine retention time and optimize fragmentation patterns.

Quantification of c-di-GMP in *B. cenocepacia* biofilm cells

Freezer stocks were revived overnight in T-soy broth and then grown for 24 h in M9 minimal medium + 3% galactose (GMM) at 37 ˚C. 1.25 mL of each strain was added to 125 mL 3% GMM in a flask containing 100 7-mm polystyrene beads and incubated at 100 rpm at 37 ˚C for 12 h. While harvesting, flasks were incubated on ice for 10 min. For the biofilm phase, the planktonic culture was discarded, and the beads were washed with 60 mL of cold PBS. These were then divided into four 50 mL centrifuge tubes containing 20 mL of cold PBS each. Each tube was vortexed for 30 s to remove the attached cells, and the PBS from all four sets was combined. The samples were then serially diluted and plated in half-strength T-soy X-gal plates to enumerate CFU/flask and then centrifuged at max speed for 15 min at 25 ˚C. Pellets were then resuspended in 500 μL of ice-cold extraction buffer (methanol:acetonitrile:dH_2O 40:40:20 + 0.1 N formic acid). The suspensions were transferred to 1.5-mL microfuge tubes and incubated at −20 ˚C for 1 h, followed by 95 ˚C for 10 min. The tubes were then centrifuged to pellet the cell debris. 400 μL of the liquid phase was transferred to another microfuge tube and 16 μL of neutralization buffer (15% ammonium bicarbonate) was added. The tubes were stored at

−80 ˚C. Quantification of c-di-GMP using mass spectroscopy was then carried out, as previously described [70].

Quantification of c-di-GMP in *B. cenocepacia* planktonic cells

Freezer stocks were revived overnight in T-soy broth and then grown for 24 h in M9 minimal medium + 3% galactose (GMM) at 37 ˚C. 1.25 mL of each strain was added to 125 mL 3% GMM and incubated at 100 rpm at 37 ˚C for 12 h. While harvesting, flasks were incubated on ice for 10 min. The samples were then serially diluted and plated in half-strength T-soy plates to enumerate CFU/flask and then centrifuged at max speed for 15 min at 4 ˚C. Pellets were then resuspended in 500 μL of ice-cold extraction buffer (methanol:acetonitrile:dH_2O 40:40:20 + 0.1 N formic acid). The suspensions were transferred to 1.5-mL microfuge tubes and incubated at −20 ˚C for 1 h, followed by 95 ˚C for 10 min. The tubes were then centrifuged to pellet the cell debris. 400 μL of the liquid phase was transferred to another microfuge tube and 16 μL of neutralization buffer (15% ammonium bicarbonate) was added. The tubes were stored at −80 ˚C. Quantification of c-di-GMP using mass spectroscopy was then carried out, as previously described [70].

Lipid analysis

Unknown lipids were extracted from $RpfR_{Ct}$(PAS) for analysis, as described previously [17,71]. A 2:1 mixture of chloroform and methanol was added to purified $RpfR_{Ct}$(PAS) in buffer I in a 4:1 ratio. The solution was then mixed vigorously until $RpfR_{Ct}$(PAS) had precipitated. The different phases were allowed to separate, and the chloroform layer was removed for analysis.

Lipid released from purified $RpfR_{Ct}$(PAS) was determined by the analysis of the purified protein extract on an Agilent 6120 LC-MS system equipped with an EMD Millipore Chromolith SpeedROD analytical RP-HPLC column (50 x 4.6 mm). A 0.5 mL solution of $RpfR_{Ct}$(PAS) in buffer I was extracted using a 2-mL mixture of chloroform and methanol (2:1). The bottom organic layer was separated and concentrated using N_2 flow. The remaining residue was taken in 100 μL of acetonitrile/water (1:1), and the solution was centrifuged to remove any precipitate. 50 μL of the supernatant (or 25 μL of the standards in acetonitrile/water [4:1]) were analyzed by LC-MS using a gradient of 10%–100% acetonitrile in water containing 0.1% formic acid in 10 min at a flowrate of 1 mL/min. The identification of the lipid was determined by the presence of the negative ionization $[M\text{-}H]^-$ corresponding to either $BDSF^-$ (*m/z* calculated for $C_{12}H_{21}O_2^-$ = 197.2) or $C12{:}0^-$ (*m/z* calculated for $C_{12}H_{23}O_2^-$ = 199.3) anions as observed in the extracted ion chromatogram of the lipids *m/z*.

Lipid released from purified $RpfR_{Ct}$(PAS) that was coexpressed with $RpfF_{Bc}$, was identified by following the same extraction protocol described above. For LC-MS analysis, a gradient of 40%–100% acetonitrile in water containing 0.1% formic acid in 10 min at a flowrate of 1 mL/min was used to improve the separation between BDSF and C12:0 signals.

BDSF production assay

Starter cultures of individual strains to be tested were incubated overnight at 37 ˚C and 200 RPM in 10 g LB (IBI Scientific) per 1 L diH_2O. In order to remove residual BDSF, starter cultures were pelleted at 15,000 RPM at 25 ˚C for 10 min. Supernatants were removed from pelleted cells, which were twice resuspended in fresh LB. 25 mL of sterile LB was inoculated with 50 μL of starter culture and grown for 33 h at 37 ˚C and 200 RPM. Aliquots of the culture were removed at the specified times. To obtain cell-free supernatants, culture samples were centrifuged for 5 min at 15,000 RPM at 25 ˚C. Supernatants were separated from the pelleted

samples and centrifuged for an additional 5 min at 15,000 RPM at 25 ˚C and stored at −20 ˚C. Aliquots were diluted and grown on LB agar plates overnight at 37 ˚C in order to determine the number of colony forming units (CFU) at the specified time.

BDSF production was measured with the *B*. *cenocepacia* H111 pAN-L15 reporter strain using a modified protocol similar to those reported in [20,41]. The reporter strain was grown for 18 h in LB supplemented with 100 μg/mL kanamycin and 80 μg/mL chloramphenicol at 37 ˚C and 200 RPM to an OD_{600} = 1.6–2.5. The reporter strain was pelleted at 3,000 × g for 30 min at 25 ˚C and resuspended twice in fresh LB supplemented with 100 μg/mL kanamycin and 80 μg/mL chloramphenicol. 100 μL of reporter strain was added to individual wells of a 96-well flat clear-bottom black polystyrene TC-treated microplate (Costar). Cell-free supernatants from individual donor strain samples were diluted 1:10 (v/v) in fresh LB supplemented with 100 μg/mL kanamycin and 80 μg/mL chloramphenicol. 100 μL of the diluted donor strain cell-free supernatant was added to a well containing 100 μL of the reporter strain and incubated at 30 ˚C for 22 h. Following incubation, 50 μL decyl aldehyde (Sigma-Aldrich) was added to the lid of the microplate. Samples were shaken for 1 min at 200 RPM prior to measuring cell density (OD_{570}), and light counts per second (CPS) for each sample were measured using a Perkin Elmer Envision 2014 plate reader equipped for advanced luminometry to determine relative light units (RLU) for each sample. RLU is defined as CPS/OD_{570}. Relative Bioluminescence is defined as RLU/CFU.

Production of full-length wild-type $RpfR_{Bc}$, $RpfR_{Bc}$–S168A, $RpfR_{Bc}$–N171A, $RpfR_{Bc}$–R186A, and $RpfR_{Bc}$–N201A

Full-length *rpfR*$_{Bc}$ (corresponding to amino acids 1–667) was amplified using Phusion High-Fidelity DNA Polymerase from WT *B*. *cenocepacia* HI2424 genomic DNA and the oligonucleotide pair primer 7 and primer 16. The PCR amplified insert was gel purified and cloned into a SapI/XhoI linearized pTB146 vector using In-Fusion (Takara Bio, USA) to generate pHis6-SUMO-$RpfR_{Bc}$(full). Individual BDSF-binding site mutations (S168A, N171A, R186A, and N201A) were introduced into pHis6-SUMO-$RpfR_{Bc}$(full) using the QuikChange II Site Directed Mutagenesis Kit (Agilent Technologies) and the mutagenic primer pairs S168AF, S168AR, N171AF, N171AR, R186AF, R186AR, N201AF, and N201AR (S2 Table).

The full-length wild-type $RpfR_{Bc}$, $RpfR_{Bc}$–S168A, $RpfR_{Bc}$–N171A, $RpfR_{Bc}$–R186A, and $RpfR_{Bc}$–N201A expression vectors were transformed into *E*. *coli strain* BL21(DE3) cells and grown to OD_{600} = 0.60 in LB containing 100 μM ampicillin at 37 ˚C and 220 RPM, then moved to 25 ˚C and 200 RPM and induced with 500 μM IPTG. Cells were grown for an additional 16 h at 25 ˚C and 200 RPM and harvested by centrifugation at 3,000 × g for 30 min at 4 ˚C. Full-length wild-type $RpfR_{Bc}$, $RpfR_{Bc}$–S168A, $RpfR_{Bc}$–N171A, $RpfR_{Bc}$–R186A, and $RpfR_{Bc}$–N201A were purified in an identical manner. The pelleted cells were resuspended in buffer T (100 mM NaCl, 50 mM MOPS [pH 7.0], 10 μg/mL DNAse, and 1 mM PMSF) and lysed by two passages through a French press at approximately 25,000 PSI. The lysate was clarified at 35,000 × g for 60 min at 4 ˚C. 100 μL His_6-Ulp1 was added to 500 μL clarified lysate and incubated at 4 ˚C for 1 h. Following the incubation, the reaction was centrifuged at 15,000 RPM for 5 min at 25 ˚C, and the pre- and post-Ulp1 digested samples were evaluated by SDS-PAGE.

Supporting information

S1 Fig. Identification of the lipid molecule released from purified $RpfR_{Ct}$(PAS) as C12:0. The LC-MS ionization traces of (A) total ions and (B) the extracted ion chromatogram of C12:0 in the $RpfR_{Ct}$(PAS) domain protein extract. (C) The mass spectrum corresponding to

the C12:0 ion peak showing the negative ionization of the lipid (red arrow). The numerical values underlying panels A and B can be found in S1 Data. C12:0, dodecanoic acid; LC-MS, liquid chromatography–mass spectrometry; PAS, Per-Arnt-Sim; RpfR, regulation of pathogenicity factor R.
(TIF)

S2 Fig. Amino acid sequence conservation among RpfR homologues. (A) An amino acid alignment and consensus sequence for conserved residues of the PAS domain from RpfR homologues was generated using CLC Sequence Viewer Version 8 (CLC bio, Aarhus, Denmark). Residues interacting with the carboxylic acid group of either C12:0 or BDSF are highlighted blue. The highly conserved Asn202 that interacts with C3 of BDSF is highlighted in yellow. The residues comprising the hydrophobic acyl–binding pocket are surrounded by unfilled black boxes. The secondary structure representation of RpfR(PAS) was determined using the PyMOL algorithm and is shown below the consensus sequence. (Purple cylinders are α-helices and pink arrows are β-strands. Disordered residues are depicted as a dashed black line.) [72] (B) An amino acid alignment and consensus sequence for conserved residues of the FI domain from RpfR homologues was generated using CLC Sequence Viewer Version 8 (CLC bio, Aarhus, Denmark). Nonconserved residues are marked with asterisks. Residues interacting with RpfF are surrounded by black boxes, with residues forming hydrogen bonds or salt bridges highlighted in blue. Interacting residues were determined by analyzing the $RpfR_{Ct}$(FI)–$RpfF_{Bc}$ structure using the PISA and PDBsum servers [73,74]. The secondary structure representation of RpfR(FI) was determined using the PyMOL algorithm and is shown below the consensus sequence. (Purple cylinders are α-helices and pink arrows are β-strands.) [72] Asn, asparagine; BDSF, *Burkholderia* DSF; C3, carbon 3; C12:0, dodecanoic acid; FI, RpfF interaction; PAS, Per-Arnt-Sim; PDB, Protein Data Bank; PISA, Proteins, interfaces, structures, and assemblies; RpfF, regulation of pathogenicity factor F; RpfR, regulation of pathogenicity factor R.
(TIF)

S3 Fig. BDSF is released from purified $RpfR_{Ct}$(PAS) coexpressed with $RpfF_{Bc}$. (A) Ligand released from $RpfR_{Ct}$(PAS) coexpressed with $RpfF_{Bc}$ was analyzed by LC-MS, and the extracted ion chromatograms are shown for the m/z corresponding to BDSF (black curve) and C12:0 (yellow curve). For comparison, a mixture containing both BDSF (200 μM) and C12:0 (200 μM) standards was analyzed by LC-MS, and the extracted ion chromatograms are shown for the m/z corresponding to BDSF (orange curve) and C12:0 (blue curve). (B) The mass spectrum corresponding to the BDSF ion peak showing the negative ionization of the lipid (red arrow) released from $RpfR_{Ct}$(PAS) coexpressed with $RpfF_{Bc}$. The numerical values underlying panel A can be found in S1 Data. BDSF, *Burkholderia* DSF; C12:0, dodecanoic acid; LC-MS, liquid chromatography–mass spectrometry; PAS, Per-Arnt-Sim; RpfF, regulation of pathogenicity factor F; RpfR, regulation of pathogenicity factor R.
(TIF)

S4 Fig. Schematic representation of the $RpfR_{Ct}$(PAS)–BDSF interface. BDSF (sticks) is shown bound to $RpfR_{Ct}$(PAS). Carbon atoms are colored black, oxygen atoms red, nitrogen atoms blue, and hydrogen atoms colored the same color as the atom to which they are bonded. H-bonds are depicted as dashed blue lines alongside measured distances (distances are not drawn to scale). The interaction between the BDSF and Asn202 is shown as an orange dashed line connecting the Asn202 sidechain nitrogen, with the closest BDSF carbon (C3) alongside its measured distance. The hydrophobic-binding pocket is depicted as a blue line. This molecular graphic was produced with Poseview [75]. Asn, asparagine BDSF, *Burkholderia* DSF; C3,

carbon 3; PAS, Per-Arnt-Sim; RpfR, regulation of pathogenicity factor R.
(TIF)

S5 Fig. Full-length wild-type $RpfR_{Bc}$, $RpfR_{Bc}$–S168A, $RpfR_{Bc}$–N171A, $RpfR_{Bc}$–R186A, and $RpfR_{Bc}$–N201A are comparably soluble. SDS-PAGE analysis of full-length wild-type $RpfR_{Bc}$, $RpfR_{Bc}$–S168A, $RpfR_{Bc}$–N171A, $RpfR_{Bc}$–R186A, and $RpfR_{Bc}$–N201A before and after 1 h 4 ˚C incubation with His_6-Ulp1 SUMO protease. *M* protein size marker (kD). RpfR, regulation of pathogenicity factor R; SUMO, small ubiquitin-like modifier.
(TIF)

S6 Fig. $RpfR_{Ct}$(FI) is structurally distinct from PAS and GAF domains. (A) $RpfR_{Ct}$(FI) is shown alongside the top-scoring PDBeFold and DALI server hits for PAS and GAF domains, (B) the KinA PAS-A domain (PDB: 2VLG) [76], and (C) the GAF domain of Dcsbis (PDB: 4ZMU). Structures are shown depicted as cartoon (top) and topological (bottom) models. All secondary structure elements are labeled and colored accordingly: cyan α-helix, magenta β-strand, and peach linker. Cache,Ca^{2+}channels-chemotaxis receptors; DALI, Distance-matrix alignment; FI, RpfF interaction; GAF, cyclic GMP-specific phosphodiesterase-adenylyl cyclase-FhlA; PAS, Per-Arnt-Sim; PDB, Protein Data Bank; RpfR, regulation of pathogenicity factor R.
(TIF)

S7 Fig. Purification of His_6-SUMO-$RpfR_{Bc}$(FI-PAS)-$RpfF_{Bc}$. SDS-PAGE analysis of Ni column purification fractions. *M* protein size marker (kD), minus preinduction sample, plus postinduction sample, *P* pellet, *S* clarified lysate supernatant, *F* flow through, *W* wash, E_1–E_4 elutions with increasing concentrations of imidazole, *R* eluted Ni resin. Bands corresponding to His_6-SUMO-$RpfR_{Bc}$(FI-PAS) and $RpfF_{Bc}$ are surrounded by red boxes. FI, RpfF interaction; PAS, Per-Arnt-Sim; RpfF, regulation of pathogenicity factor F; RpfR, regulation of pathogenicity factor R; SUMO, small ubiquitin-like modifier.
(TIF)

S8 Fig. The amino acid sequence of RpfF homologues from various gram-negative species. An alignment of the amino acid sequences of RpfF from several gram-negative species that also contain an adjacent RpfR homologue are shown above a consensus sequence for identical residues (residues that are not conserved are depicted as *s). Alignment and consensus sequences were generated using CLC Sequence Viewer Version 8 (CLC bio, Aarhus, Denmark). Residues interacting with RpfR(FI) are surrounded by black boxes with residues forming a salt bridge or hydrogen-bonding interaction with RpfR(FI) highlighted blue. Secondary structure elements determined using the PyMOL algorithm [72] are shown below their corresponding sequence elements. (Orange cylinders are α-helices and green arrows are β-strands. Disordered residues are depicted as a dashed black line.) FI, RpfF interaction; RpfF, regulation of pathogenicity factor F; RpfR, regulation of pathogenicity factor R.
(TIF)

S9 Fig. In the presence of $RpfR_{Ct}$(FI), the $RpfF_{Bc}$ substrate tunnel is devoid of fatty acid. (A) Alignment of $RpfF_{Bc}$ from the $RpfF_{Bc}$–$RpfR_{Ct}$(FI) complex (gold) ($RpfR_{Ct}$[FI] and a bound glycerol molecule are omitted for clarity) with $RpfF_{Bc}$ alone (green) (PDB: 5FUS) [17], which contains a molecule of C12:0 present in its active site that copurified with the protein. (B) Expanded view of the area enclosed by the rectangle in A following a 20˚ rotation, depicting the movement of residues Phe44 and Phe88 (green and gold sticks) into space occupied by C12:0 (pink/red balls and grey sticks) in $RpfF_{Bc}$ alone. C12:0, dodecanoic acid; FI, RpfF interaction; PDB, Protein Data Bank; Phe, phenylalanine; RpfF, regulation of pathogenicity factor

F; RpfR, regulation of pathogenicity factor R.
(TIF)

S1 Table. Phasing and refinement statistics. $R_{sym} = \Sigma_h \Sigma_i | I_i(h) - \langle I(h) \rangle | / \Sigma_h \Sigma_i I_i(h)$, in which $I_i(h)$ is the i^{th} measurement of h and $\langle I(h) \rangle$ is the mean for all measurements of I(h) for reflection h. $R_{work} = \Sigma ||F_o| - |F_c|| / \Sigma |F_o|$ was calculated with a working set of reflections. R_{free} is R_{work} calculated using a test set of reflections. Data for the highest-resolution shells are in parentheses. Each data set was collected from a single crystal.
(DOC)

S2 Table. Oligonucleotides.
(DOC)

S1 Data. Excel spreadsheet containing the numerical data and analysis for Figs 2G, 2H, 4B, 6A, 6B and 6C; and S1A, S1B and S3A Figs.
(XLSX)

Acknowledgments

We gratefully acknowledge Valerie J. Carabetta for assistance in constructing the pHis7-Acp-P_{Ec}/N-AcpS_{Ec} expression vector as well as helpful discussions; David Dubnau, Glenn C. Capodagli, Atul Khataokar, Eisha Mhatre, Faisal Tarique Khaja, and Ian Campbell for helpful discussions and critical assessment of the manuscript; Shao-Gang Li for help with LC-MS; and Holger K. Moustakas for helpful discussions. The DSF reporter strain was graciously provided by Leo Eberl. X-ray diffraction data were collected at the Stanford Synchrotron Light Source beamlines 14–1 and 9–2.

Author Contributions

Conceptualization: Evan J. Waldron, Christopher M. Waters, Vaughn S. Cooper, Matthew B. Neiditch.

Data curation: Evan J. Waldron, Daniel Snyder, Nicolas L. Fernandez, Daigo Inoyama, Joel S. Freundlich, Christopher M. Waters, Vaughn S. Cooper, Matthew B. Neiditch.

Formal analysis: Evan J. Waldron, Daniel Snyder, Nicolas L. Fernandez, Daigo Inoyama, Joel S. Freundlich, Christopher M. Waters, Vaughn S. Cooper, Matthew B. Neiditch.

Funding acquisition: Christopher M. Waters, Vaughn S. Cooper, Matthew B. Neiditch.

Investigation: Evan J. Waldron, Daniel Snyder, Nicolas L. Fernandez, Emily Sileo, Daigo Inoyama, Joel S. Freundlich, Christopher M. Waters, Vaughn S. Cooper, Matthew B. Neiditch.

Methodology: Evan J. Waldron, Daniel Snyder, Nicolas L. Fernandez, Daigo Inoyama, Joel S. Freundlich, Christopher M. Waters, Vaughn S. Cooper, Matthew B. Neiditch.

Project administration: Joel S. Freundlich, Christopher M. Waters, Vaughn S. Cooper, Matthew B. Neiditch.

Resources: Evan J. Waldron, Daniel Snyder, Nicolas L. Fernandez, Christopher M. Waters, Vaughn S. Cooper, Matthew B. Neiditch.

Supervision: Joel S. Freundlich, Christopher M. Waters, Vaughn S. Cooper, Matthew B. Neiditch.

Validation: Evan J. Waldron, Daniel Snyder, Nicolas L. Fernandez, Daigo Inoyama, Joel S. Freundlich, Christopher M. Waters, Vaughn S. Cooper, Matthew B. Neiditch.

Visualization: Evan J. Waldron, Daniel Snyder, Nicolas L. Fernandez, Daigo Inoyama, Joel S. Freundlich, Christopher M. Waters, Vaughn S. Cooper, Matthew B. Neiditch.

Writing – original draft: Evan J. Waldron, Daniel Snyder, Nicolas L. Fernandez, Daigo Inoyama, Joel S. Freundlich, Christopher M. Waters, Vaughn S. Cooper, Matthew B. Neiditch.

Writing – review & editing: Evan J. Waldron, Daniel Snyder, Nicolas L. Fernandez, Daigo Inoyama, Joel S. Freundlich, Christopher M. Waters, Vaughn S. Cooper, Matthew B. Neiditch.

References

1. Waters CM, Bassler BL. Quorum sensing: cell-to-cell communication in bacteria. Annu Rev Cell Dev Biol. 2005; 21:319–46. Epub 2005/10/11. https://doi.org/10.1146/annurev.cellbio.21.012704.131001 PMID: 16212498.
2. Ng WL, Bassler BL. Bacterial quorum-sensing network architectures. Annu Rev Genet. 2009; 43:197–222. Epub 2009/08/19. https://doi.org/10.1146/annurev-genet-102108-134304 PMID: 19686078.
3. Jimenez JC, Federle MJ. Quorum sensing in group A Streptococcus. Front Cell Infect Microbiol. 2014; 4:127. Epub 2014/10/14. https://doi.org/10.3389/fcimb.2014.00127 PMID: 25309879; PubMed Central PMCID: PMC4162386.
4. Neiditch MB, Capodagli GC, Prehna G, Federle MJ. Genetic and Structural Analyses of RRNPP Intercellular Peptide Signaling of Gram-Positive Bacteria. Annu Rev Genet. 2017. Epub 2017/09/07. https://doi.org/10.1146/annurev-genet-120116-023507 PMID: 28876981.
5. Papenfort K, Bassler BL. Quorum sensing signal-response systems in Gram-negative bacteria. Nat Rev Microbiol. 2016; 14(9):576–88. Epub 2016/08/12. https://doi.org/10.1038/nrmicro.2016.89 PMID: 27510864; PubMed Central PMCID: PMCPMC5056591.
6. Dow JM. Diffusible signal factor-dependent quorum sensing in pathogenic bacteria and its exploitation for disease control. J Appl Microbiol. 2017; 122(1):2–11. Epub 2016/09/30. https://doi.org/10.1111/jam.13307 PMID: 27684652.
7. Boon C, Deng Y, Wang LH, He Y, Xu JL, Fan Y, et al. A novel DSF-like signal from Burkholderia cenocepacia interferes with Candida albicans morphological transition. ISME J. 2008; 2(1):27–36. Epub 2007/12/01. https://doi.org/10.1038/ismej.2007.76 PMID: 18049456.
8. Deng Y, Boon C, Chen S, Lim A, Zhang LH. Cis-2-dodecenoic acid signal modulates virulence of Pseudomonas aeruginosa through interference with quorum sensing systems and T3SS. BMC Microbiol. 2013; 13:231. Epub 2013/10/19. https://doi.org/10.1186/1471-2180-13-231 PMID: 24134835; PubMed Central PMCID: PMCPMC4016476.
9. Barber CE, Tang JL, Feng JX, Pan MQ, Wilson TJ, Slater H, et al. A novel regulatory system required for pathogenicity of Xanthomonas campestris is mediated by a small diffusible signal molecule. Mol Microbiol. 1997; 24(3):555–66. Epub 1997/05/01. PMID: 9179849.
10. Traverse CC, Mayo-Smith LM, Poltak SR, Cooper VS. Tangled bank of experimentally evolved Burkholderia biofilms reflects selection during chronic infections. Proc Natl Acad Sci U S A. 2013; 110(3):E250–9. Epub 2012/12/29. https://doi.org/10.1073/pnas.1207025110 PMID: 23271804; PubMed Central PMCID: PMCPMC3549113.
11. Silva IN, Santos PM, Santos MR, Zlosnik JE, Speert DP, Buskirk SW, et al. Long-Term Evolution of Burkholderia multivorans during a Chronic Cystic Fibrosis Infection Reveals Shifting Forces of Selection. mSystems. 2016; 1(3). Epub 2016/11/09. https://doi.org/10.1128/mSystems.00029-16 PMID: 27822534; PubMed Central PMCID: PMCPMC5069766.
12. Zhou L, Zhang LH, Camara M, He YW. The DSF Family of Quorum Sensing Signals: Diversity, Biosynthesis, and Turnover. Trends Microbiol. 2017; 25(4):293–303. Epub 2016/12/17. https://doi.org/10.1016/j.tim.2016.11.013 PMID: 27979499.
13. Wang LH, He Y, Gao Y, Wu JE, Dong YH, He C, et al. A bacterial cell-cell communication signal with cross-kingdom structural analogues. Mol Microbiol. 2004; 51(3):903–12. Epub 2004/01/21. PMID: 14731288.
14. Davies DG, Marques CN. A fatty acid messenger is responsible for inducing dispersion in microbial biofilms. J Bacteriol. 2009; 191(5):1393–403. Epub 2008/12/17. https://doi.org/10.1128/JB.01214-08 PMID: 19074399; PubMed Central PMCID: PMCPMC2648214.

15. Bi H, Christensen QH, Feng Y, Wang H, Cronan JE. The Burkholderia cenocepacia BDSF quorum sensing fatty acid is synthesized by a bifunctional crotonase homologue having both dehydratase and thioesterase activities. Mol Microbiol. 2012; 83(4):840–55. Epub 2012/01/10. https://doi.org/10.1111/j.1365-2958.2012.07968.x PMID: 22221091; PubMed Central PMCID: PMCPMC3276249.

16. Zhou L, Yu Y, Chen X, Diab AA, Ruan L, He J, et al. The Multiple DSF-family QS Signals are Synthesized from Carbohydrate and Branched-chain Amino Acids via the FAS Elongation Cycle. Sci Rep. 2015; 5:13294. Epub 2015/08/21. https://doi.org/10.1038/srep13294 PMID: 26289160; PubMed Central PMCID: PMCPMC4542539.

17. Spadaro F, Scoffone VC, Chiarelli LR, Fumagalli M, Buroni S, Riccardi G, et al. The Crystal Structure of Burkholderia cenocepacia DfsA Provides Insights into Substrate Recognition and Quorum Sensing Fatty Acid Biosynthesis. Biochemistry. 2016; 55(23):3241–50. Epub 2016/05/21. https://doi.org/10.1021/acs.biochem.6b00178 PMID: 27198181.

18. Cheng Z, He YW, Lim SC, Qamra R, Walsh MA, Zhang LH, et al. Structural basis of the sensor-synthase interaction in autoinduction of the quorum sensing signal DSF biosynthesis. Structure. 2010; 18(9):1199–209. Epub 2010/09/10. https://doi.org/10.1016/j.str.2010.06.011 PMID: 20826346.

19. Liu L, Li T, Cheng XJ, Peng CT, Li CC, He LH, et al. Structural and functional studies on Pseudomonas aeruginosa DspI: implications for its role in DSF biosynthesis. Sci Rep. 2018; 8(1):3928. Epub 2018/03/04. https://doi.org/10.1038/s41598-018-22300-1 PMID: 29500457; PubMed Central PMCID: PMCPMC5834635.

20. Suppiger A, Eshwar AK, Stephan R, Kaever V, Eberl L, Lehner A. The DSF type quorum sensing signalling system RpfF/R regulates diverse phenotypes in the opportunistic pathogen Cronobacter. Sci Rep. 2016; 6:18753. Epub 2016/01/05. https://doi.org/10.1038/srep18753 PMID: 26725701; PubMed Central PMCID: PMCPMC4698668.

21. Lindenberg S, Klauck G, Pesavento C, Klauck E, Hengge R. The EAL domain protein YciR acts as a trigger enzyme in a c-di-GMP signalling cascade in E. coli biofilm control. EMBO J. 2013; 32(14):2001–14. Epub 2013/05/28. https://doi.org/10.1038/emboj.2013.120 PMID: 23708798; PubMed Central PMCID: PMCPMC3715855.

22. Deng Y, Schmid N, Wang C, Wang J, Pessi G, Wu D, et al. Cis-2-dodecenoic acid receptor RpfR links quorum-sensing signal perception with regulation of virulence through cyclic dimeric guanosine monophosphate turnover. Proc Natl Acad Sci U S A. 2012; 109(38):15479–84. Epub 2012/09/06. https://doi.org/10.1073/pnas.1205037109 PMID: 22949660; PubMed Central PMCID: PMC3458384.

23. Moglich A, Ayers RA, Moffat K. Structure and signaling mechanism of Per-ARNT-Sim domains. Structure. 2009; 17(10):1282–94. Epub 2009/10/20. https://doi.org/10.1016/j.str.2009.08.011 PMID: 19836329; PubMed Central PMCID: PMCPMC3092527.

24. Henry JT, Crosson S. Ligand-binding PAS domains in a genomic, cellular, and structural context. Annu Rev Microbiol. 2011; 65:261–86. Epub 2011/06/15. https://doi.org/10.1146/annurev-micro-121809-151631 PMID: 21663441; PubMed Central PMCID: PMCPMC3298442.

25. Jenal U, Reinders A, Lori C. Cyclic di-GMP: second messenger extraordinaire. Nat Rev Microbiol. 2017; 15(5):271–84. Epub 2017/02/07. https://doi.org/10.1038/nrmicro.2016.190 PMID: 28163311.

26. Newman KL, Almeida RP, Purcell AH, Lindow SE. Cell-cell signaling controls Xylella fastidiosa interactions with both insects and plants. Proc Natl Acad Sci U S A. 2004; 101(6):1737–42. Epub 2004/02/03. https://doi.org/10.1073/pnas.0308399100 PMID: 14755059; PubMed Central PMCID: PMCPMC341844.

27. Chatterjee S, Newman KL, Lindow SE. Cell-to-cell signaling in Xylella fastidiosa suppresses movement and xylem vessel colonization in grape. Mol Plant Microbe Interact. 2008; 21(10):1309–15. Epub 2008/09/13. https://doi.org/10.1094/MPMI-21-10-1309 PMID: 18785826.

28. Daniels MJ, Barber CE, Turner PC, Sawczyc MK, Byrde RJ, Fielding AH. Cloning of genes involved in pathogenicity of Xanthomonas campestris pv. campestris using the broad host range cosmid pLAFR1. EMBO J. 1984; 3(13):3323–8. Epub 1984/12/20. PMID: 16453595; PubMed Central PMCID: PMCPMC557857.

29. Dow JM, Crossman L, Findlay K, He YQ, Feng JX, Tang JL. Biofilm dispersal in Xanthomonas campestris is controlled by cell-cell signaling and is required for full virulence to plants. Proc Natl Acad Sci U S A. 2003; 100(19):10995–1000. Epub 2003/09/10. https://doi.org/10.1073/pnas.1833360100 PMID: 12960398; PubMed Central PMCID: PMCPMC196915.

30. Deng Y, Wu J, Eberl L, Zhang LH. Structural and functional characterization of diffusible signal factor family quorum-sensing signals produced by members of the Burkholderia cepacia complex. Appl Environ Microbiol. 2010; 76(14):4675–83. Epub 2010/06/01. https://doi.org/10.1128/AEM.00480-10 PMID: 20511428; PubMed Central PMCID: PMCPMC2901730.

31. Dean SN, Chung MC, van Hoek ML. Burkholderia Diffusible Signal Factor Signals to Francisella novicida To Disperse Biofilm and Increase Siderophore Production. Appl Environ Microbiol. 2015; 81

(20):7057–66. Epub 2015/08/02. https://doi.org/10.1128/AEM.02165-15 PMID: 26231649; PubMed Central PMCID: PMCPMC4579433.

32. Udine C, Brackman G, Bazzini S, Buroni S, Van Acker H, Pasca MR, et al. Phenotypic and genotypic characterisation of Burkholderia cenocepacia J2315 mutants affected in homoserine lactone and diffusible signal factor-based quorum sensing systems suggests interplay between both types of systems. PLoS One. 2013; 8(1):e55112. Epub 2013/02/06. https://doi.org/10.1371/journal.pone.0055112 PMID: 23383071; PubMed Central PMCID: PMCPMC3557247.

33. Oursel D, Loutelier-Bourhis C, Orange N, Chevalier S, Norris V, Lange CM. Identification and relative quantification of fatty acids in Escherichia coli membranes by gas chromatography/mass spectrometry. Rapid Commun Mass Spectrom. 2007; 21(20):3229–33. Epub 2007/09/11. https://doi.org/10.1002/rcm.3177 PMID: 17828792.

34. Hengge R. Trigger phosphodiesterases as a novel class of c-di-GMP effector proteins. Philos Trans R Soc Lond B Biol Sci. 2016; 371(1707). Epub 2016/09/28. https://doi.org/10.1098/rstb.2015.0498 PMID: 27672149; PubMed Central PMCID: PMCPMC5052742.

35. Poltak SR, Cooper VS. Ecological succession in long-term experimentally evolved biofilms produces synergistic communities. ISME J. 2011; 5(3):369–78. Epub 2010/09/03. https://doi.org/10.1038/ismej.2010.136 PMID: 20811470; PubMed Central PMCID: PMCPMC3105725.

36. Orengo CA, Michie AD, Jones S, Jones DT, Swindells MB, Thornton JM. CATH—a hierarchic classification of protein domain structures. Structure. 1997; 5(8):1093–108. Epub 1997/08/15. PMID: 9309224.

37. Schutt CE, Myslik JC, Rozycki MD, Goonesekere NC, Lindberg U. The structure of crystalline profilin-beta-actin. Nature. 1993; 365(6449):810–6. Epub 1993/10/28. https://doi.org/10.1038/365810a0 PMID: 8413665.

38. Upadhyay AA, Fleetwood AD, Adebali O, Finn RD, Zhulin IB. Cache Domains That are Homologous to, but Different from PAS Domains Comprise the Largest Superfamily of Extracellular Sensors in Prokaryotes. PLoS Comput Biol. 2016; 12(4):e1004862. Epub 2016/04/07. https://doi.org/10.1371/journal.pcbi.1004862 PMID: 27049771; PubMed Central PMCID: PMCPMC4822843.

39. Ho YS, Burden LM, Hurley JH. Structure of the GAF domain, a ubiquitous signaling motif and a new class of cyclic GMP receptor. EMBO J. 2000; 19(20):5288–99. Epub 2000/10/18. https://doi.org/10.1093/emboj/19.20.5288 PMID: 11032796; PubMed Central PMCID: PMCPMC314001.

40. Altschul SF, Gish W, Miller W, Myers EW, Lipman DJ. Basic local alignment search tool. J Mol Biol. 1990; 215(3):403–10. Epub 1990/10/05. https://doi.org/10.1016/S0022-2836(05)80360-2 PMID: 2231712.

41. Suppiger A, Aguilar C, Eberl L. Evidence for the widespread production of DSF family signal molecules by members of the genus Burkholderia by the aid of novel biosensors. Environ Microbiol Rep. 2016; 8(1):38–44. Epub 2015/10/22. https://doi.org/10.1111/1758-2229.12348 PMID: 26487448.

42. Almeida RP, Killiny N, Newman KL, Chatterjee S, Ionescu M, Lindow SE. Contribution of rpfB to cell-to-cell signal synthesis, virulence, and vector transmission of Xylella fastidiosa. Mol Plant Microbe Interact. 2012; 25(4):453–62. Epub 2011/12/30. https://doi.org/10.1094/MPMI-03-11-0074 PMID: 22204646.

43. Bi H, Yu Y, Dong H, Wang H, Cronan JE. Xanthomonas campestris RpfB is a fatty Acyl-CoA ligase required to counteract the thioesterase activity of the RpfF diffusible signal factor (DSF) synthase. Mol Microbiol. 2014; 93(2):262–75. Epub 2014/05/29. https://doi.org/10.1111/mmi.12657 PMID: 24866092; PubMed Central PMCID: PMCPMC4114240.

44. Barends TR, Hartmann E, Griese JJ, Beitlich T, Kirienko NV, Ryjenkov DA, et al. Structure and mechanism of a bacterial light-regulated cyclic nucleotide phosphodiesterase. Nature. 2009; 459(7249):1015–8. Epub 2009/06/19. https://doi.org/10.1038/nature07966 PMID: 19536266.

45. Sundriyal A, Massa C, Samoray D, Zehender F, Sharpe T, Jenal U, et al. Inherent regulation of EAL domain-catalyzed hydrolysis of second messenger cyclic di-GMP. J Biol Chem. 2014; 289(10):6978–90. Epub 2014/01/24. https://doi.org/10.1074/jbc.M113.516195 PMID: 24451384; PubMed Central PMCID: PMCPMC3945359.

46. Winkler A, Udvarhelyi A, Hartmann E, Reinstein J, Menzel A, Shoeman RL, et al. Characterization of elements involved in allosteric light regulation of phosphodiesterase activity by comparison of different functional BlrP1 states. J Mol Biol. 2014; 426(4):853–68. Epub 2013/12/03. https://doi.org/10.1016/j.jmb.2013.11.018 PMID: 24291457; PubMed Central PMCID: PMCPMC3989770.

47. Rao F, Qi Y, Chong HS, Kotaka M, Li B, Li J, et al. The functional role of a conserved loop in EAL domain-based cyclic di-GMP-specific phosphodiesterase. J Bacteriol. 2009; 191(15):4722–31. Epub 2009/04/21. https://doi.org/10.1128/JB.00327-09 PMID: 19376848; PubMed Central PMCID: PMCPMC2715702.

48. Liu C, Liew CW, Wong YH, Tan ST, Poh WH, Manimekalai SMS, et al. Insights into biofilm dispersal regulation from the crystal structure of the PAS-GGDEF-EAL region of RbdA from Pseudomonas

aeruginosa. J Bacteriol. 2017. Epub 2017/11/08. https://doi.org/10.1128/JB.00515-17 PMID: 29109186; PubMed Central PMCID: PMCPMC5763044.

49. Bendezu FO, Hale CA, Bernhardt TG, de Boer PA. RodZ (YfgA) is required for proper assembly of the MreB actin cytoskeleton and cell shape in E. coli. EMBO J. 2009; 28(3):193–204. Epub 2008/12/17. https://doi.org/10.1038/emboj.2008.264 PMID: 19078962; PubMed Central PMCID: PMCPMC2637328.

50. Wilkins MR, Gasteiger E, Bairoch A, Sanchez JC, Williams KL, Appel RD, et al. Protein identification and analysis tools in the ExPASy server. Methods Mol Biol. 1999; 112:531–52. Epub 1999/02/23. PMID: 10027275.

51. Strub MP, Hoh F, Sanchez JF, Strub JM, Bock A, Aumelas A, et al. Selenomethionine and selenocysteine double labeling strategy for crystallographic phasing. Structure. 2003; 11(11):1359–67. Epub 2003/11/08. PMID: 14604526.

52. Otwinowski Z, Minor W. [20] Processing of X-ray diffraction data collected in oscillation mode. Methods in enzymology. 1997; 276:307–26. Epub 1997/01/01. https://doi.org/10.1016/S0076-6879(97)76066-X PMID: 27799103.

53. Terwilliger TC, Adams PD, Read RJ, McCoy AJ, Moriarty NW, Grosse-Kunstleve RW, et al. Decision-making in structure solution using Bayesian estimates of map quality: the PHENIX AutoSol wizard. Acta crystallographica Section D, Biological crystallography. 2009; 65(Pt 6):582–601. Epub 2009/05/26. https://doi.org/10.1107/S0907444909012098 PMID: 19465773; PubMed Central PMCID: PMCPMC2685735.

54. Terwilliger TC, Grosse-Kunstleve RW, Afonine PV, Moriarty NW, Zwart PH, Hung LW, et al. Iterative model building, structure refinement and density modification with the PHENIX AutoBuild wizard. Acta crystallographica Section D, Biological crystallography. 2008; 64(Pt 1):61–9. Epub 2007/12/21. https://doi.org/10.1107/S090744490705024X PMID: 18094468; PubMed Central PMCID: PMCPMC2394820.

55. Emsley P, Lohkamp B, Scott WG, Cowtan K. Features and development of Coot. Acta crystallographica Section D, Biological crystallography. 2010; 66(Pt 4):486–501. Epub 2010/04/13. https://doi.org/10.1107/S0907444910007493 PMID: 20383002; PubMed Central PMCID: PMCPMC2852313.

56. Adams PD, Grosse-Kunstleve RW, Hung LW, Ioerger TR, McCoy AJ, Moriarty NW, et al. PHENIX: building new software for automated crystallographic structure determination. Acta crystallographica Section D, Biological crystallography. 2002; 58(Pt 11):1948–54. Epub 2002/10/24. PMID: 12393927.

57. McCoy AJ, Grosse-Kunstleve RW, Adams PD, Winn MD, Storoni LC, Read RJ. Phaser crystallographic software. Journal of applied crystallography. 2007; 40(Pt 4):658–74. Epub 2007/08/01. https://doi.org/10.1107/S0021889807021206 PMID: 19461840; PubMed Central PMCID: PMCPMC2483472.

58. Stevenson SR, Kamisugi Y, Trinh CH, Schmutz J, Jenkins JW, Grimwood J, et al. Genetic Analysis of Physcomitrella patens Identifies ABSCISIC ACID NON-RESPONSIVE, a Regulator of ABA Responses Unique to Basal Land Plants and Required for Desiccation Tolerance. Plant Cell. 2016; 28(6):1310–27. Epub 2016/05/20. https://doi.org/10.1105/tpc.16.00091 PMID: 27194706; PubMed Central PMCID: PMCPMC4944411.

59. Afonine PV, Grosse-Kunstleve RW, Echols N, Headd JJ, Moriarty NW, Mustyakimov M, et al. Towards automated crystallographic structure refinement with phenix.refine. Acta crystallographica Section D, Biological crystallography. 2012; 68(Pt 4):352–67. Epub 2012/04/17. https://doi.org/10.1107/S0907444912001308 PMID: 22505256; PubMed Central PMCID: PMCPMC3322595.

60. Moriarty NW, Grosse-Kunstleve RW, Adams PD. electronic Ligand Builder and Optimization Workbench (eLBOW): a tool for ligand coordinate and restraint generation. Acta crystallographica Section D, Biological crystallography. 2009; 65(Pt 10):1074–80. Epub 2009/09/23. https://doi.org/10.1107/S0907444909029436 PMID: 19770504; PubMed Central PMCID: PMCPMC2748967.

61. Cronan JE, Thomas J. Bacterial fatty acid synthesis and its relationships with polyketide synthetic pathways. Methods in enzymology. 2009; 459:395–433. Epub 2009/04/14. https://doi.org/10.1016/S0076-6879(09)04617-5 PMID: 19362649; PubMed Central PMCID: PMCPMC4095770.

62. Jiang Y, Chan CH, Cronan JE. The soluble acyl-acyl carrier protein synthetase of Vibrio harveyi B392 is a member of the medium chain acyl-CoA synthetase family. Biochemistry. 2006; 45(33):10008–19. Epub 2006/08/16. https://doi.org/10.1021/bi060842w PMID: 16906759.

63. Masoudi A, Raetz CR, Zhou P, Pemble CWt. Chasing acyl carrier protein through a catalytic cycle of lipid A production. Nature. 2014; 505(7483):422–6. Epub 2013/11/08. https://doi.org/10.1038/nature12679 PMID: 24196711; PubMed Central PMCID: PMCPMC3947097.

64. Scheich C, Kummel D, Soumailakakis D, Heinemann U, Bussow K. Vectors for co-expression of an unrestricted number of proteins. Nucleic Acids Res. 2007; 35(6):e43. Epub 2007/02/22. https://doi.org/10.1093/nar/gkm067 PMID: 17311810; PubMed Central PMCID: PMCPMC1874614.

65. Marcella AM, Jing F, Barb AW. Preparation of holo- and malonyl-[acyl-carrier-protein] in a manner suitable for analog development. Protein Expr Purif. 2015; 115:39–45. Epub 2015/05/27. https://doi.org/10.1016/j.pep.2015.05.013 PMID: 26008118.

66. Fazli M, Harrison JJ, Gambino M, Givskov M, Tolker-Nielsen T. In-Frame and Unmarked Gene Deletions in Burkholderia cenocepacia via an Allelic Exchange System Compatible with Gateway Technology. Appl Environ Microbiol. 2015; 81(11):3623–30. Epub 2015/03/22. https://doi.org/10.1128/AEM.03909-14 PMID: 25795676; PubMed Central PMCID: PMCPMC4421043.

67. Baym M, Kryazhimskiy S, Lieberman TD, Chung H, Desai MM, Kishony R. Inexpensive multiplexed library preparation for megabase-sized genomes. PLoS One. 2015; 10(5):e0128036. Epub 2015/05/23. https://doi.org/10.1371/journal.pone.0128036 PMID: 26000737; PubMed Central PMCID: PMCPMC4441430.

68. Deatherage DE, Barrick JE. Identification of mutations in laboratory-evolved microbes from next-generation sequencing data using breseq. Methods Mol Biol. 2014; 1151:165–88. Epub 2014/05/20. https://doi.org/10.1007/978-1-4939-0554-6_12 PMID: 24838886; PubMed Central PMCID: PMCPMC4239701.

69. Cooper VS. Experimental Evolution as a High-Throughput Screen for Genetic Adaptations. mSphere. 2018; 3(3). Epub 2018/05/11. https://doi.org/10.1128/mSphere.00121-18 PMID: 29743200.

70. Massie JP, Reynolds EL, Koestler BJ, Cong JP, Agostoni M, Waters CM. Quantification of high-specificity cyclic diguanylate signaling. Proc Natl Acad Sci U S A. 2012; 109(31):12746–51. Epub 2012/07/18. https://doi.org/10.1073/pnas.1115663109 PMID: 22802636; PubMed Central PMCID: PMCPMC3411991.

71. Montersino S, Orru R, Barendregt A, Westphal AH, van Duijn E, Mattevi A, et al. Crystal structure of 3-hydroxybenzoate 6-hydroxylase uncovers lipid-assisted flavoprotein strategy for regioselective aromatic hydroxylation. J Biol Chem. 2013; 288(36):26235–45. Epub 2013/07/19. https://doi.org/10.1074/jbc.M113.479303 PMID: 23864660; PubMed Central PMCID: PMCPMC3764827.

72. DeLano WL. The PyMOL Molecular Graphics System (DeLano Scientific, San Carlos, CA). 2002.

73. Krissinel E, Henrick K. Inference of macromolecular assemblies from crystalline state. J Mol Biol. 2007; 372(3):774–97. Epub 2007/08/08. https://doi.org/10.1016/j.jmb.2007.05.022 PMID: 17681537.

74. Laskowski RA, Hutchinson EG, Michie AD, Wallace AC, Jones ML, Thornton JM. PDBsum: a Web-based database of summaries and analyses of all PDB structures. Trends Biochem Sci. 1997; 22(12):488–90. Epub 1998/01/20. PMID: 9433130.

75. Stierand K, Rarey M. From modeling to medicinal chemistry: automatic generation of two-dimensional complex diagrams. Chemmedchem. 2007; 2(6):853–60. Epub 2007/04/17. https://doi.org/10.1002/cmdc.200700010 PMID: 17436259.

76. Lee J, Tomchick DR, Brautigam CA, Machius M, Kort R, Hellingwerf KJ, et al. Changes at the KinA PAS-A dimerization interface influence histidine kinase function. Biochemistry. 2008; 47(13):4051–64. Epub 2008/03/08. https://doi.org/10.1021/bi7021156 PMID: 18324779.